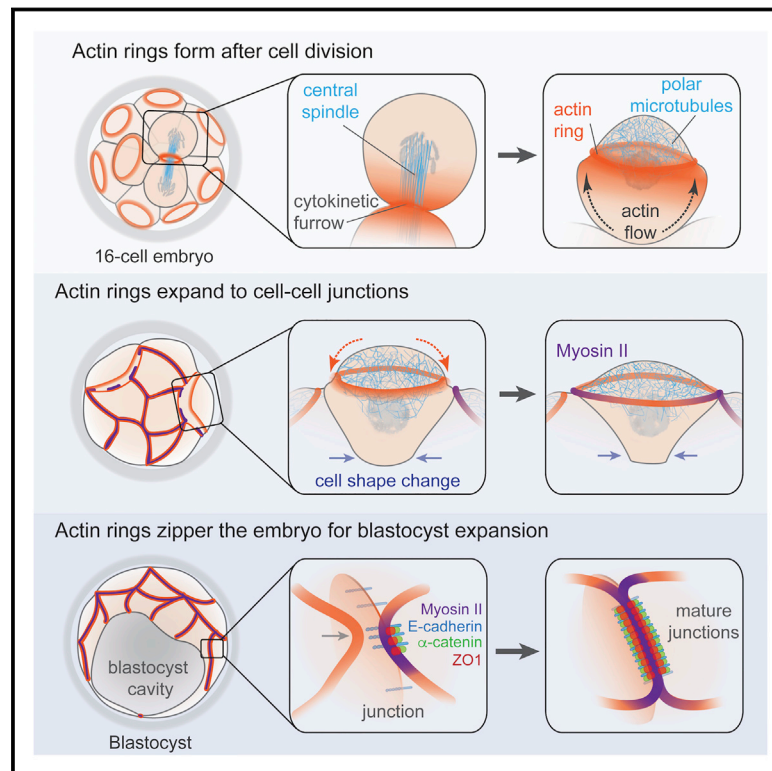


Expanding Actin Rings Zipper the Mouse Embryo for Blastocyst Formation

Graphical Abstract



Authors

Jennifer Zenker, Melanie D. White, Maxime Gasnier, ..., Stephanie Bissiere, Maté Biro, Nicolas Plachta

Correspondence

m.biro@unsw.edu.au (M.B.),
plachtan@imcb.a-star.edu.sg (N.P.)

In Brief

Expanding actin rings zipper the mouse embryo to seal it and allow formation of the blastocyst cavity.

Highlights

- Cortical flows and polar microtubules interact to form actin rings following division
- Actin rings expand to cell-cell junctions
- Coupling of actin rings stabilizes adherens and tight junctions
- Actin rings zipper along junctions to seal the embryo for blastocyst formation



Expanding Actin Rings Zipper the Mouse Embryo for Blastocyst Formation

Jennifer Zenker,^{1,6} Melanie D. White,^{1,6} Maxime Gasnier,^{1,6} Yanina D. Alvarez,^{1,2,6} Hui Yi Grace Lim,¹ Stephanie Bissiere,¹ Maté Biro,^{3,4,7,*} and Nicolas Plachta^{1,5,7,8,*}

¹Institute of Molecular and Cell Biology, A*STAR, Singapore

²Facultad de Ciencias Exactas y Naturales, Universidad de Buenos Aires, CONICET, Buenos Aires, Argentina

³EMBL Australia, Single Molecule Science node, School of Medical Sciences, University of New South Wales, Sydney, Australia

⁴ARC Centre of Excellence in Advanced Molecular Imaging, University of New South Wales, Sydney, Australia

⁵Department of Biochemistry, National University of Singapore, Singapore

⁶These authors contributed equally

⁷Senior author

⁸Lead Contact

*Correspondence: m.biro@unsw.edu.au (M.B.), plachtan@imcb.a-star.edu.sg (N.P.)

<https://doi.org/10.1016/j.cell.2018.02.035>

SUMMARY

Transformation from morula to blastocyst is a defining event of preimplantation embryo development. During this transition, the embryo must establish a paracellular permeability barrier to enable expansion of the blastocyst cavity. Here, using live imaging of mouse embryos, we reveal an actin-zipping mechanism driving this embryo sealing. Preceding blastocyst stage, a cortical F-actin ring assembles at the apical pole of the embryo's outer cells. The ring structure forms when cortical actin flows encounter a network of polar microtubules that exclude F-actin. Unlike stereotypical actin rings, the actin rings of the mouse embryo are not contractile, but instead, they expand to the cell-cell junctions. Here, they couple to the junctions by recruiting and stabilizing adherens and tight junction components. Coupling of the actin rings triggers localized myosin II accumulation, and it initiates a tension-dependent zipping mechanism along the junctions that is required to seal the embryo for blastocyst formation.

INTRODUCTION

During the preimplantation stage of mammalian development, the cells of the embryo assemble adherens and tight junctions to establish the first forms of tissue architecture (White et al., 2017; Yamanaka et al., 2006). E-cadherin (E-cad) trans-ligation at adherens junctions enables a mechanical coupling of the cell cortices of neighboring cells and promotes cell-cell adhesion (Samarage et al., 2015; Stephenson et al., 2010). Tight junctions create a permeability barrier that seals the embryo from the exterior (Eckert and Fleming, 2008). The establishment of this barrier allows for an increase in osmotically driven hydrostatic pressure in the space between cells, thereby expanding the first internal

cavity of the embryo and transforming the morula into a blastocyst.

Although initial studies suggested that the mouse embryo becomes sealed after the 32-cell stage when the embryo transforms into a blastocyst (McLaren and Smith, 1977), subsequent work indicated that the sealing process is initiated earlier. The latter model is supported by (1) the enrichment of adherens and tight junction components in outer cells of the embryo during the 16- to 32-cell-stage transition, (2) defects in blastocyst formation due to perturbation of adherens and tight junctions, and (3) functional assays using freely diffusing dextrans that demonstrate the establishment of an epithelial barrier prior to the 32-cell stage (Ducibella et al., 1975; Moriwaki et al., 2007; Watson and Barcroft, 2001). Despite progress in the identification of molecular components required for blastocyst formation, the morphogenetic mechanism that triggers embryo sealing remains unknown.

In most tissues and organs, morphogenesis is driven via the coordinated coupling of adherens and tight junctions to cellular actin networks (Heisenberg and Bellaïche, 2013; Lecuit et al., 2011). However, it is unclear how actin networks in the early mammalian embryo might contribute to sealing or blastocyst formation. Here we imaged filamentous actin (F-actin) in living mouse embryos to uncover mechanisms required for embryo sealing. We show that F-actin rings appear at the apical cortex of the outer cells of the embryo, then expand to cell-cell junctions where they undergo zipping, triggering sealing of the embryo and enabling blastocyst formation.

RESULTS

Cortical F-Actin Rings Expand and Zipper along Cell-Cell Junctions before Blastocyst Formation

To visualize F-actin non-invasively, we imaged intact live mouse embryos expressing GFP fused to Utraphin (GFP-Utr) (Burkel et al., 2007) during the 16- to 32-cell stage. GFP-Utr strongly labeled an actin ring-like structure at the apical cortex of the outer cells (Figures 1A and 1B). This ring encloses a region typically described as the apical domain (Johnson and Maro, 1984). The



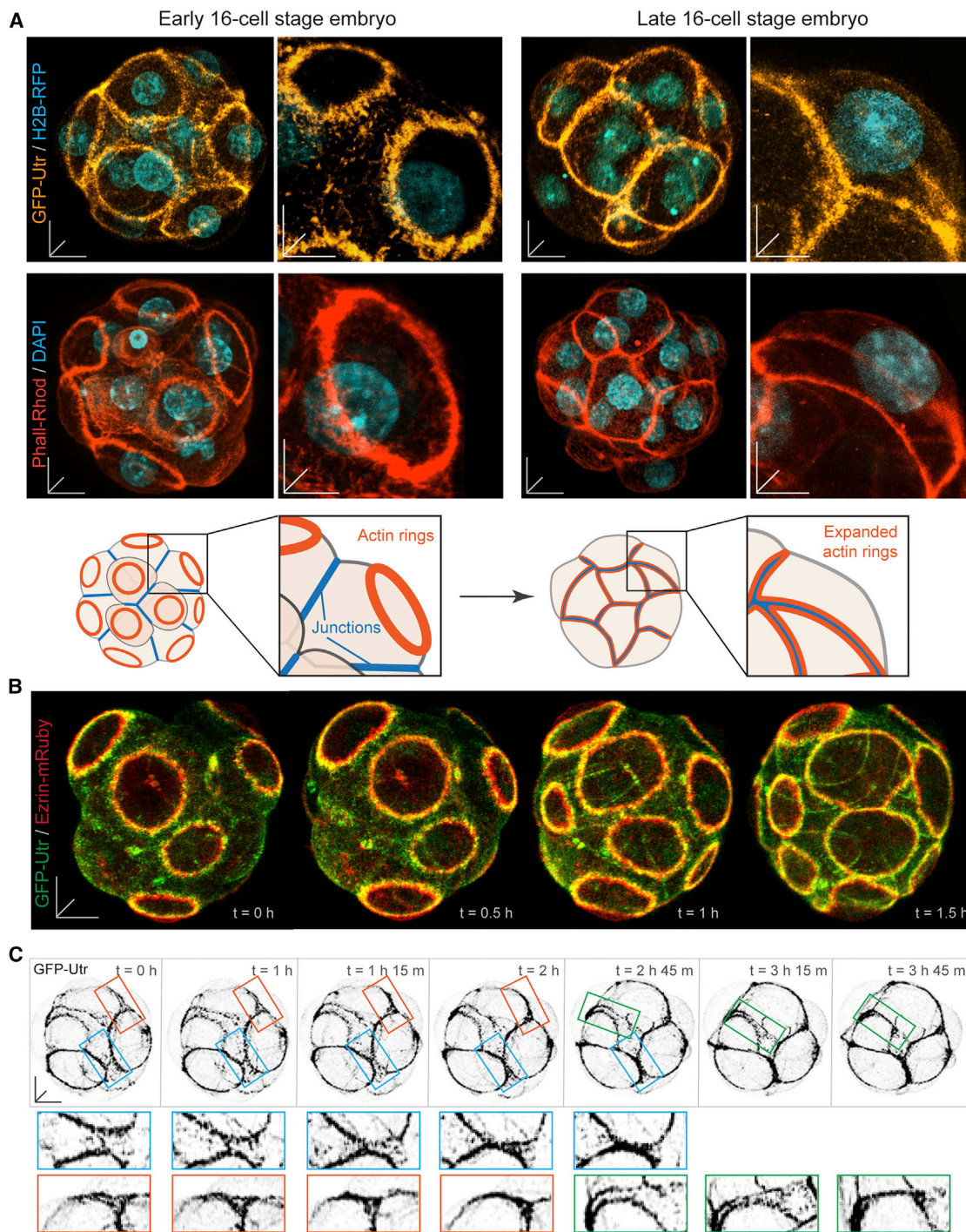


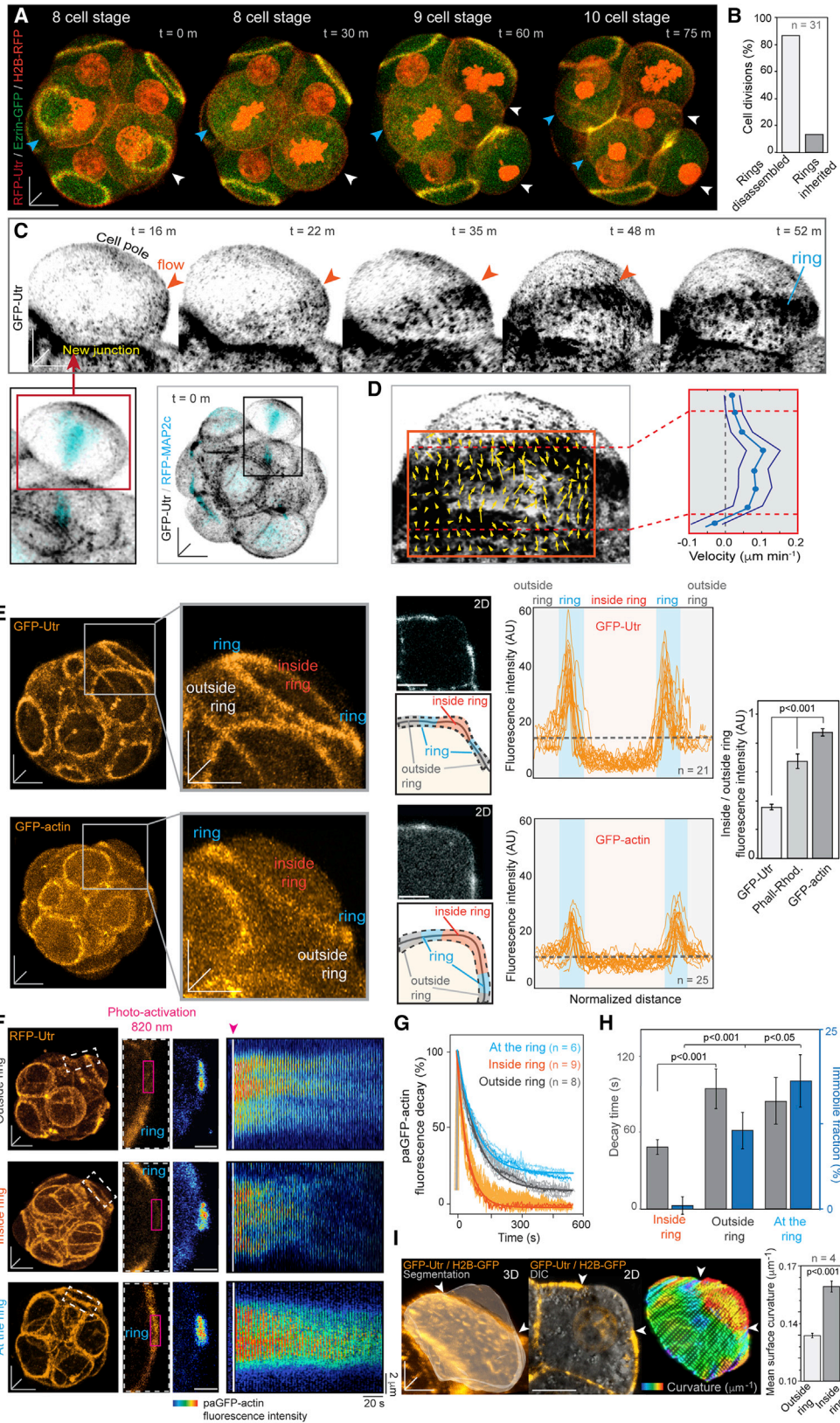
Figure 1. Cortical F-Actin Rings Expand and Zipper before Blastocyst Formation

(A) Actin rings at the apical cortex of cells in live (GFP-Utrophin) and fixed (Phalloidin-Rhodamine) embryos. Schematic shows actin rings before and after expansion and zipping along junctions.

(B) Actin rings expand to junctions during the 16-cell stage in a live embryo.

(C) Actin rings zipper simultaneously at multiple junctions in a live embryo. Boxes show three regions where actin rings make contact and zipper.

Scale bars, 10 μ m.



(legend on next page)

ring was also labeled in live embryos by the membrane-to-cortex attachment protein Ezrin fused to mRuby (Ezrin-mRuby), the actin bundler Fascin fused to Emerald (Emerald-Fascin), and the scaffolding protein Pard6b fused to GFP (GFP-Pard6b) and in fixed embryos stained with Phalloidin-Rhodamine or for endogenous phosphorylated Ezrin (pEzrin) (Figures 1A, 1B, and S1A–S1E).

Actin rings typically drive diverse morphogenetic processes by constriction (Schwayer et al., 2016). However, instead of constricting, the rings of the mouse embryo expanded over the entire apical cortex to the cell-cell junctions during the 16- to 32-cell stage (Figures 1A, 1B, and S1A–S1E; Movie S1). Moreover, following their expansion, the rings of neighboring cells formed an initial point of contact at the shared junction. Once established, this contact extended bidirectionally along the junctions in a zippering-like process, which formed a unified linear structure connecting the adjoining cells (Figures 1B and 1C; Movie S1).

Zippering of actin rings occurred simultaneously at multiple junctions during the 16- to 32-cell stage (Figures 1C and S1A). Furthermore, when cells divided after the 32-cell stage, the daughter cells did not form a new actin ring. Instead, they retained their zippered architecture during division and blastocyst expansion (Figures S1F and S1G). As the expansion of the rings and their zippering occurred just prior to the blastocyst stage, it may serve as a mechanism to seal the embryo for blastocyst formation. Therefore, we investigated which processes drive actin ring formation, expansion, and zippering.

Cortical Flows Drive Actin Ring Formation *De Novo* at the 16-Cell Stage

Although actin rings only zipper after the 16-cell stage, similar structures enclose the apical domain in 8-cell embryos (Johnson and Maro, 1984) (Figure 2A). It is asserted that these regions are asymmetrically segregated during the division of 8-cell-stage blastomeres to determine daughter cell fate (Chazaud et al., 2006; Hirate et al., 2015; Leung et al., 2016; Maître et al., 2016; Yamanaka et al., 2006). However, imaging divisions in intact 8-cell embryos showed that the majority of rings labeled by apical domain markers RFP-Utr, Ezrin-GFP, GFP-Pard6b, atypical protein kinase C isoform PKC ζ (aPKC-Emerald), or the apical surface marker Lck-GFP disassembled prior to cytokinesis (87.1%, $n = 31$ cell divisions) (Figures 2A, 2B, and S2A–S2D; Movie S2), and most cells assembled an actin ring *de novo* after

cytokinesis (Figures 2C and S2D). These results were confirmed in uninjected embryos stained for Phalloidin-Rhodamine and pEzrin (Figure S2E). Moreover, the few cells that did not establish an actin ring *de novo* resulted from divisions in which the ring was either asymmetrically inherited or disassembled before cytokinesis (Figure S2F). We do not exclude the possibility that some unknown components of the apical domain may be asymmetrically retained during division. However, we propose that the localization of apical polarity markers is most frequently reestablished rather than directly inherited following division, consistent with previous observations (Anani et al., 2014; Watanabe et al., 2014). Therefore, we determined which processes are responsible for the *de novo* formation of the ring at the 16-cell stage.

As the actin ring forms following cytokinesis, we imaged cells at a high temporal resolution in embryos expressing GFP-Utr and fluorescently tagged microtubule-associated protein 2c (RFP-MAP2c) (Figure 2C). These experiments revealed a flow of cortical F-actin commencing at the end of cytokinesis (Figure 2C; Movie S3). Particle image velocimetry (PIV) analysis (Mayer et al., 2010) demonstrated that the flow initiates at the region where the cytokinetic furrow disassembles and a nascent cell-cell junction is formed, and is directed toward the cell poles (Figure 2D). Using a multiphoton laser to label photoactivatable GFP fused to actin (paGFP-actin) at the cell cortex of the nascent junction also demonstrated a directional flow toward the cell pole (Figures S2G and S2H).

The flow did not replenish GFP-Utr uniformly across the cell cortex. Instead, it was interrupted at the edge of a spherical cap largely devoid of GFP-Utr, indicating an exclusion zone for stable cortical F-actin. The flow caused a progressive accumulation of GFP-Utr at the edge of this exclusion zone, resulting in the formation of a ring-like structure rich in F-actin (Figures 2C, S2G, and S2H). Disruption of cortical flows by external crosslinking via wheat germ agglutinin (WGA) treatment (Canman and Bement, 1997; Sedzinski et al., 2011) prevented actin ring formation (Figure S2I). In contrast to GFP-Utr and Phalloidin-Rhodamine, actin fused to GFP (GFP-actin) was found at similar levels at the cell cortex inside and outside the ring (Figures 2E and S2J), suggesting that these regions experience different F-actin turnover rates. Therefore, we measured paGFP-actin dynamics at the cortex inside, outside, and at the ring using fluorescence decay after photoactivation (FDAP) (Plachta et al., 2011). paGFP-actin

Figure 2. Actin Rings Form *De Novo* at the 16-Cell Stage via Cortical Flows

(A and B) Live imaging (A) and quantification (B) of cell divisions in an 8-cell-stage embryo. Two cells (white and blue arrowheads) disassemble their cortical F-actin rings prior to cell division, and daughter cells (arrowheads) do not inherit an actin ring. The majority of actin rings are disassembled prior to cell division. (C) The actin ring forms *de novo* in 16-cell-stage blastomeres. Imaging live 16-cell-stage blastomeres at the end of cytokinesis reveals a flow of GFP-Utr from the nascent junction toward the cell pole. Top row shows the flow of cortical material. Arrowhead indicates region where the flow is interrupted and the actin ring starts to form.

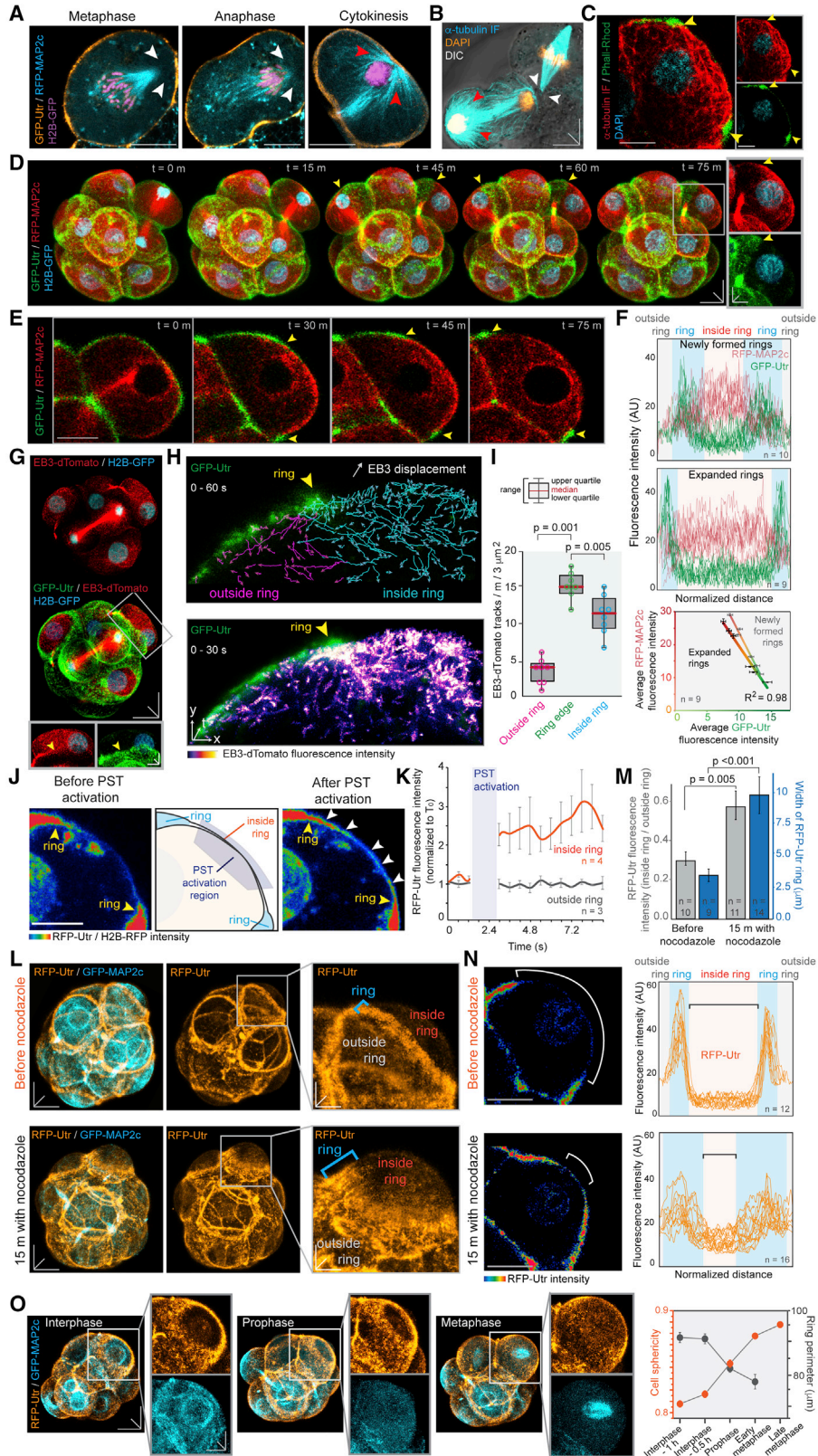
(D) Characterization of cortical flow in the cell shown in (C) using PIV analysis.

(E) Comparison between GFP-Utr and GFP-actin distribution at the cell cortex in live embryos. Whereas the cortex inside the ring is largely devoid of GFP-Utr, GFP-actin is distributed evenly inside and outside the ring. Graphs show fluorescence intensities along the cortex and comparison of GFP-Utr, Phalloidin-Rhodamine, and GFP-actin.

(F) Selective paGFP-actin photoactivation at the cortex inside, outside, and at the ring. Kymographs show paGFP-actin dynamics following photoactivation (arrowhead).

(G and H) FDAP analysis of paGFP-actin dynamics (G) reveals a faster decay time and smaller immobile fraction (H) at the cortex inside the ring compared to outside or at the ring.

(I) Formation of a membranous bulge inside the actin ring. Quantification of surface curvature reveals a more curved surface inside than outside the actin ring. Data in (D), (E), (H), and (I) are presented as mean \pm SEM. Scale bars, 10 μ m in all images except for insets in (F), 3 μ m; $n =$ cells.



(legend on next page)

displayed the fastest decay rate and the lowest immobile fraction inside the ring, confirming that there was more rapid actin turnover and fewer stable actin filaments in this region of the apical cortex (Figures 2F–2H). Furthermore, photoactivation of a selective pool of paGFP-actin at the ring showed that this paGFP-actin was retained at the ring for at least 1 hr, reflecting a stable incorporation of paGFP-actin into actin filaments at the ring (Figure S2K). These observations suggest differences in G- to F-actin ratios inside and outside the actin ring, with the pool inside the ring turning over more rapidly.

As the cortex inside the ring is largely devoid of stable F-actin, it comprises a weak area of the apical surface (Charras and Paluch, 2008). In line with this, this region formed a prominent membranous bulge similar to a cellular bleb, known to buffer intracellular pressure (Sedzinski et al., 2011) (Figure 2I). Cellular blebs typically assemble a cortical actomyosin network to arrest their expansion and retract (Biro et al., 2013). By contrast, the apical bulge inside the actin ring remains clear of F-actin throughout ring expansion. These results suggest the existence of a mechanism inhibiting cortical F-actin assembly within the ring.

A Polar Microtubule Network Excludes Cortical F-Actin from Inside the Ring

As the actin rings form at the end of cytokinesis, we investigated a role for microtubules, which differentially regulate the cortex during cell division. In other systems, microtubules originate from centrosomes (Conduit et al., 2015). During cell division, midzone microtubules recruit actomyosin to the cytokinetic furrow, while astral microtubules typically inhibit cortical F-actin at the cell poles in a process known as polar relaxation (Fededa and Gerlich, 2012; White and Borisy, 1983; Wolpert, 1960). However, the early mouse embryo lacks centrosomes and microtubule dynamics remain unclear (Clift and Schuh, 2015; Howe and FitzHarris, 2013; Zenker et al., 2017). Therefore, we characterized microtubule dynamics in live embryos expressing RFP/GFP-

MAP2c. In line with the lack of centrosomes, the mitotic spindle assembles around the chromosomes (Coelho et al., 2013) without a distinct astral microtubule network. However, at the end of telophase, a polar microtubule network rapidly expanded between the newly formed cell nucleus and the apical cortex (Figures 3A and 3B; Movie S4). The localization of this network was inversely correlated with that of GFP-Utr, resulting in an apical zone rich in microtubules and poor in F-actin (Figures 3C–3F).

Labeling microtubules with the plus-end marker EB3-dTomato, or a 2G4 construct associated with dynamic and tyrosinated microtubules (Cassimeris et al., 2013), revealed that the microtubule network underlying the cortex was denser and more dynamic inside than outside the ring (Figures 3G and S3A). Moreover, tracking microtubule plus ends demonstrated greater microtubule growth inside the ring (Figures 3H, 3I, and S3B; Movie S5). This microtubule network progressively expanded to the junctions concurrent with the expansion of the actin ring (Figures 3E and 3F).

Local disruption of microtubule polymerization inside the ring, using the photoswitchable microtubule inhibitors photostatins (PSTs) (Borowiak et al., 2015; Zenker et al., 2017), triggered rapid RFP-Utr accumulation at the cortex inside the ring. Moreover, deactivation of the previously photoactivated PSTs allowed microtubule growth to resume, resulting in renewed clearance of F-actin inside the ring (Figures 3J, 3K, and S3C–S3E). By contrast, activation of PSTs outside the ring had no effect on cortical RFP-Utr levels (Figure S3F). Furthermore, global depolymerization of microtubules using nocodazole disrupted the exclusion of GFP-Utr inside the ring, thereby shrinking the apical zone devoid of GFP-Utr (Figures 3L–3N and S3G). Consistent with our microtubule perturbations, depolymerization of the microtubule network during mitotic entry in untreated 8-cell-stage blastomeres was accompanied by shrinkage and disassembly of the actin ring prior to cytokinesis (Figure 3O). These findings indicate that a polar microtubule network clears F-actin from the apical cell cortex inside the ring.

Figure 3. Polar Microtubules Exclude F-Actin from the Cortex inside the Actin Ring

- (A) Dividing cell in a live embryo expressing RFP-MAP2c, GFP-Utr, and H2B-GFP (pseudocolored). Stereotypical astral microtubules are not detected during mitosis (white arrowheads). A microtubule network forms rapidly at the cell pole during cytokinesis (red arrowheads).
- (B) Immunofluorescence in a fixed embryo shows one cell in metaphase and another undergoing cytokinesis. Note the lack of astral microtubules (white arrowheads) and the prominent polar microtubule network in the cell undergoing cytokinesis (red arrowheads).
- (C) Staining for endogenous α -tubulin, Phalloidin-Rhodamine, and DAPI demonstrates the high density of microtubules inside the actin ring (arrowheads).
- (D) Live imaging of an entire embryo expressing RFP-MAP2c, GFP-Utr, and H2B-GFP (pseudocolored) demonstrates the formation of the polar microtubule network and actin ring in two cells following division. Insets highlight exclusion of GFP-Utr from the region of the apical cell cortex occupied by the microtubules. Arrowheads indicate region where the actin rings form.
- (E) 2D planes from a live embryo show the progressive exclusion of GFP-Utr from the apical cell cortex and the expansion of the actin ring to the junctions (arrowheads indicate actin ring).
- (F) GFP-Utr and RFP-MAP2c are inversely localized in cells with newly formed actin rings and expanded rings.
- (G) Live imaging of an embryo expressing EB3-dTomato, GFP-Utr, and H2B-GFP (pseudocolored) reveals prominent localization of microtubule plus ends inside the actin ring. Arrowhead indicates actin ring.
- (H) Tracking of EB3-dTomato in the living embryo shows an increased density of growing microtubule plus ends inside and at the ring than outside the actin ring.
- (I) More EB3-dTomato tracks per minute are found inside the ring and at the edge of the ring than outside the ring.
- (J) 2D planes from a live embryo incubated with PST. Localized PST activation induces RFP-Utr accumulation at the cortex inside the actin ring (arrowheads).
- (K) RFP-Utr fluorescence intensity at the cortex inside and outside the ring following PST activation.
- (L) Live embryo expressing RFP-Utr and GFP-MAP2c before and after nocodazole treatment. Following treatment, the interior of the actin ring shrinks.
- (M) RFP-Utr fluorescence intensity at the cortex inside the ring and actin ring width before and after nocodazole.
- (N) RFP-Utr fluorescence intensities along the apical cell surface before and with nocodazole. 2D planes highlight increased RFP-Utr intensity at the cortex inside the actin ring and shrinkage of the interior of the actin ring (brackets) caused by nocodazole.
- (O) Live embryo expressing RFP-Utr and GFP-MAP2c shows division of an 8-cell-stage blastomere. The actin ring shrinks and disassembles concomitantly with depolymerization of microtubules when the cell enters mitosis.

Data in (F), (I), (K), (M), and (O) are presented as mean \pm SEM. Scale bars, 10 μ m in all images except for insets in (L), 5 μ m; n = cells.

Changes in Cell Geometry Regulate Actin Ring Expansion

We then explored how the actin ring expands to the junctions. First, we investigated whether actin polymerization drives ring expansion. Treatment with the Arp2/3 complex inhibitor CK-666 subsequent to ring formation did not prevent ring expansion (Figure S4A). A similar treatment with the pan-formin inhibitor SMIFH2 caused a reversal of cell morphology to a spherical shape and prevented ring expansion (Figures S4A and S4B). We could not uncouple the impact of SMIFH2 on formin activity from its general effects on cell shape. Nevertheless, the sum of GFP-Utr signal within the ring, an indicator of the total amount of F-actin, did not increase and the ring became thinner during expansion (Figures S4C and S4D). This suggests that additive actin polymerization is not a main driver of ring expansion. Therefore, we explored whether changes in cell shape occurring during the 16-cell stage (White et al., 2017) contribute to expansion.

Following division, outer cells in the embryo are nearly spherical in shape (Samarage et al., 2015). As the ring expands, cells contracted their basolateral region while maintaining constant volume (Figures 4A, 4B, and S4D). Similar to the effects of SMIFH2, acute treatment with an E-cad-blocking antibody (Samarage et al., 2015) caused cells to become spherical and the actin rings to shrink (Figures 4C and S4E), suggesting an association between cell shape changes and ring expansion.

During cytokinesis, contraction of a cell pole causes a hydrostatic pressure-mediated expansion and blebbing of the opposite pole (Sedzinski et al., 2011). These blebs act as pressure sinks, buffering the expansive forces directed at the cortex. Analogously, contraction of the basolateral region of the outer cells after cytokinesis would also be expected to lead to apical displacement of cytosol and an increase in the expansive force experienced by the apical pole. As for blebs, this force tends to further inflate the bulge where the cortex is weaker and widen the aperture at the bulge base (Tinevez et al., 2009), here delimited by the actin ring. We found that the bulge flattens as the basolateral region contracts (Figures 4A and 4D), suggesting that hydrostatic forces generated by cell shape changes do not principally dissipate via bulge inflation (Figure 4G). Instead, the aperture at the base of the bulge widened and the ring expanded, indicating that the ring only exerts limited resistance to deformation compared to forces opposing bulge inflation. In line with a weak resistance to deformation, we found that (1) the ring was largely devoid of myosin II (Figure 4F; Movie S5), (2) the ring did not recoil significantly following laser ablation (Movie S6), and (3) myosin II inhibition did not prevent changes in cell shape (Figures S4F and S4G) or ring expansion (Figure 4E). These results reveal that the actin ring is not contractile, and they suggest that its resistance to deformation is likely dominated by its crosslinking and frictional forces due to membrane coupling via ERM proteins, such as Ezrin.

To test the role of membrane coupling, we manipulated Ezrin, which is required for the epithelial sealing that enables blastocoel expansion (Dard et al., 2001) and provides resistance to blebbing in other systems (Diz-Muñoz et al., 2010). Ezrin-GFP overexpression slowed ring expansion and caused a significant inflation of the bulge. Conversely, Ezrin downregulation caused faster ring expansion and reduced bulge inflation (Figures 4H, 4I, and S4H). These results indicate that the actin ring offers weak resis-

tance to deformation and expands in a myosin II-independent manner as a result of changes in cell geometry.

Expanded Actin Rings Couple to Cell-Cell Junctions

We next determined how the actin ring interacts with the junctions after expansion. Immunolabeling and live imaging revealed a localized enrichment of the adherens junction proteins E-cad and α -catenin (α -cat) and the initial recruitment of the tight junction protein zona occludens 1 (ZO1) at the site of contact between the ring and the junction (Figures 5A–5C; Movies S7 and S8). Once an initial contact was established, the ring did not disconnect from this site ($n = 97$ actin rings) (Figures 5A–5C). Expression of a truncated E-cad protein unable to link to F-actin via α -cat (E-cad- Δ ICD-GFP) and downregulation of α -cat by small interfering RNA (siRNA) decreased the actin ring expansion rate, likely due to their effects on cell shape similar to those obtained with the E-cad antibody treatment (Figures 5F and 5G). However, when the delayed actin rings of these embryos arrived at the junctions, they did not couple and remained separated from the junction (Figure 5F). ZO1 downregulation did not affect ring expansion but prevented coupling to the junction (Figures 5F, 5G, and S5A), consistent with the requirement for ZO1 to stabilize tight junctions *in vitro* by coupling them to the perijunctional actin cytoskeleton (Fanning et al., 2012; Maiers et al., 2013; Van Itallie et al., 2009). Therefore, following expansion, the actin ring establishes a stable interaction with enriched junctional components.

Following coupling of the first ring to a junction, the neighboring ring coupled specifically at the same initial contact site, not randomly along the junction (Figures 5D, 5I, and 5J). During assembly of epithelial permeability barriers, coupling of circumferential actin networks or cables to junctions increases junctional tension (Lecuit and Yap, 2015; Tornavaca et al., 2015; Van Itallie et al., 2009). Consistent with this, coupling of the first actin ring triggered accumulation of myosin II at the contact site and along the ring proximal to the contact site (Figures 5D, 5E, and 5H), suggesting the emergence of contractile forces. Moreover, the expanding ring of the neighboring cell was subsequently deformed toward the initial contact site (Figures 5D, 5I, and 5J), indicating the action of a short-range pulling force on the neighboring ring ($n = 15$) mediating a ring capture mechanism. To probe this capture mechanism, we disrupted myosin II in a spatiotemporally controlled manner using the light-activatable inhibitor azido-blebbistatin (Képiró et al., 2012), when one ring is coupled to the junction and the neighboring ring is approaching. This localized disruption transiently interrupted recruitment of the second actin ring to the junction ($n = 6$) (Figures 5K and S5B). We then employed femtosecond laser ablations of the cell cortex, which can disrupt actin networks without significant membrane damage (Kiehart et al., 2000; Rauzi and Lenne, 2011; Samarage et al., 2015). Cortex laser ablation between the junction and the approaching second ring triggered a recoil of the ring away from the junction (Figure 5L). By contrast, when the ring was far from the junction, cortex ablation near the junction did not affect ring expansion (Figure S5C). Furthermore, ablation at the cortex inside an expanding actin ring did not prevent subsequent zippering (Figure S5D). Therefore, we propose that the localized increase in tension following coupling of the first ring to the junction helps to capture and align the second ring to the same contact site for more efficient zippering.

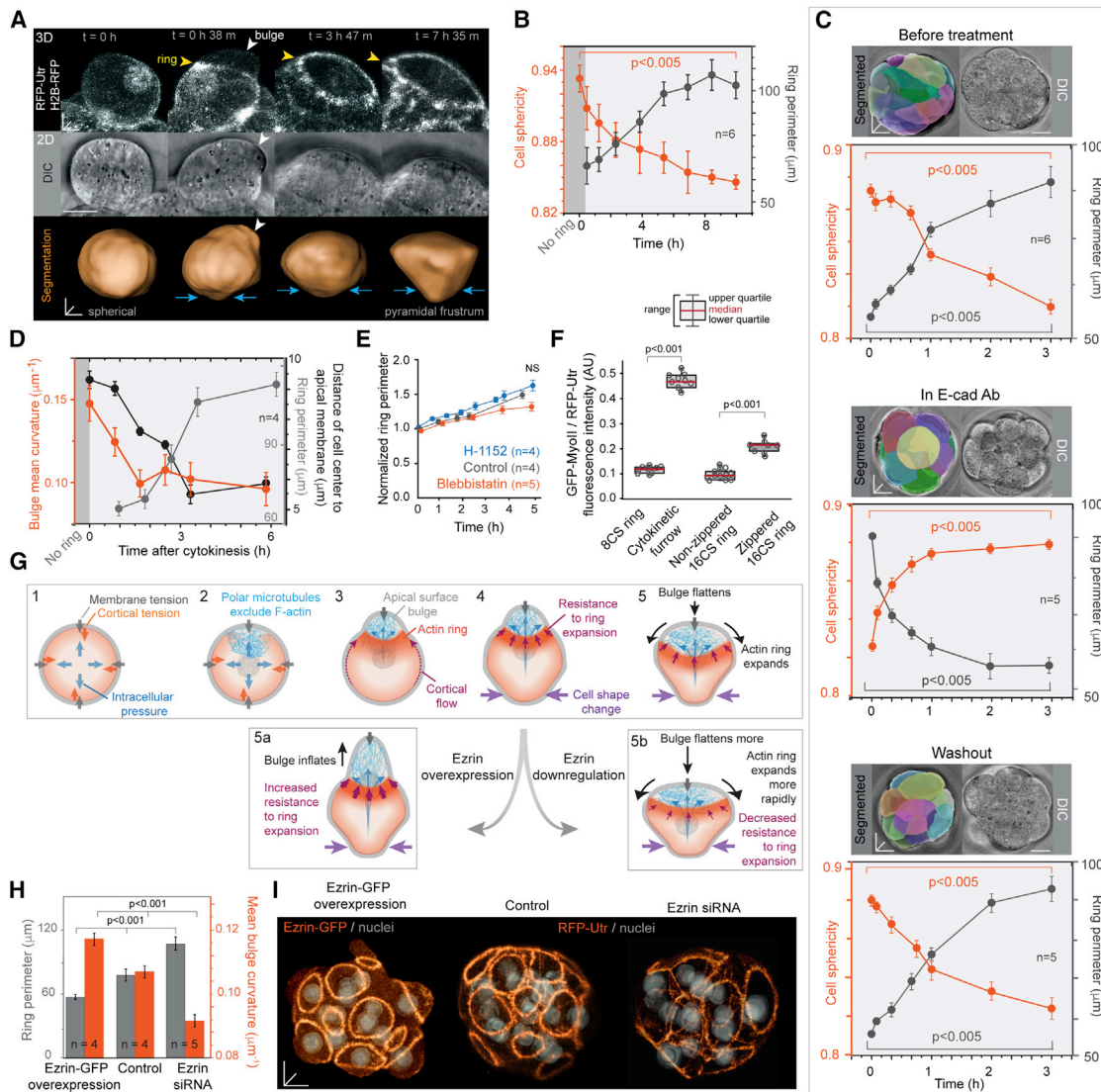


Figure 4. Actin Ring Expansion Is Associated with Changes in Cell Geometry

(A) 16-cell-stage blastomere in a live embryo. As the cell contracts its basolateral region (cyan arrows) the actin ring (yellow arrowheads) expands. The bulge inside the ring (white arrowheads) flattens as the cell changes shape.

(B) Cell sphericity and actin ring perimeter during the 16-cell stage. $T = 0$ is the onset of ring formation.

(C) Acute cell shape disruption using an E-cad antibody (E-cad Ab) induces increased cell sphericity and actin ring shrinkage. After antibody washout, cells become less spherical and actin rings expand again.

(D) Comparison of changes in bulge curvature, distance between the cell center of mass and the apical membrane (proxy for contraction of the basolateral region), and actin ring perimeter over time. The curvature of the bulge decreases as the cell changes shape and the ring expands.

(E) Actin rings still expand in embryos treated with blebbistatin or H-1152 during the 16-cell stage.

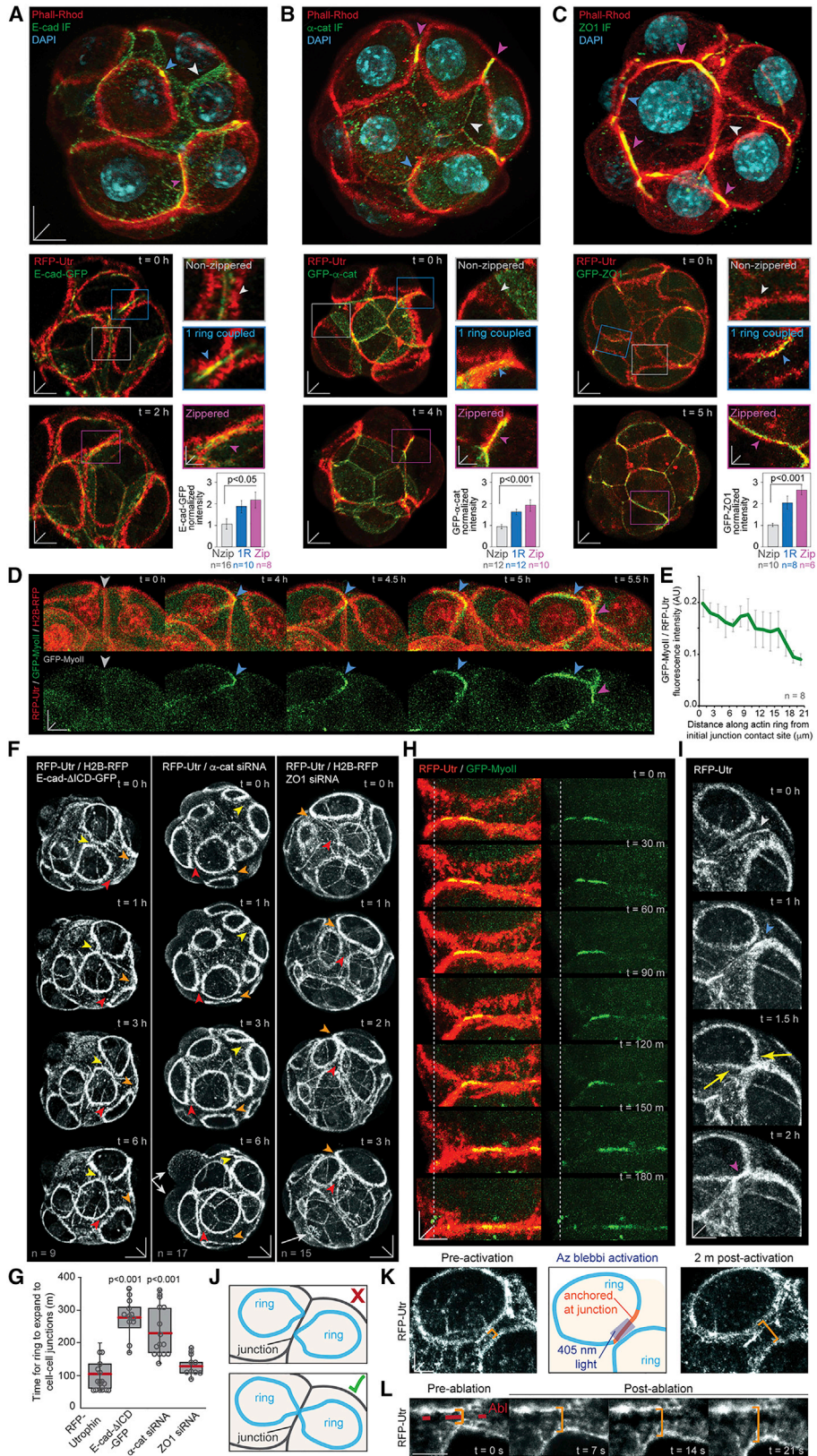
(F) GFP-MyoII intensity at the actin ring is low but increases significantly following zippering.

(G) Schematic of changes in cell shape and actin ring expansion. (1) Hydrostatic pressure within a cell is resisted by tension in the cortex and plasma membrane. (2) A network of microtubules appears after division and clears F-actin from the apical surface. (3) The apical region devoid of F-actin is weakened, as only membrane tension resists intracellular pressure, and thus a bulge forms. (4) The basolateral region progressively narrows and cytosol is displaced apically, increasing the expansive force experienced by the apical surface. (5) As the ring is not contractile, it only weakly resists deformation, favoring ring expansion and flattening of the bulge over further inflation of the bulge. (5a) Increasing the resistive force exerted by the ring by Ezrin overexpression increases bulge surface curvature. (5b) Conversely, decreasing Ezrin levels causes a more rapid widening of the ring and flattening of the bulge.

(H) Ezrin-GFP overexpression reduces ring perimeter and increases bulging.

(I) Ezrin downregulation produces larger rings with less pronounced bulges.

Data in (B)–(F) and (H) are presented as mean \pm SEM. Scale bars, 10 μm . n = embryos in (E) and (H) and cells elsewhere.



(legend on next page)

Actin Ring Zippering Is Tension Dependent

We next determined how coupled actin rings zipper along junctions. Imaging RFP-Utr, E-cad-GFP, and GFP-ZO1 demonstrated that zippering starts at the initial contact site and proceeds bidirectionally to the tricellular junctions (Figures 6A and 6B; Movies S7 and S8). GFP-MyoII accumulated along the coupled rings, and it was specifically enriched at and proximal to the advancing zipper (Figures 5D, 5E, 5H, and 6C). Upon completion of zippering, myosin II remained specifically enriched at apical junctions throughout the embryo (Figure 6C; Movie S5), suggesting that zippering requires increased line tension along the rings.

To probe tensile forces along the rings, we employed laser-based ablations (Movie S6) (Kiehart et al., 2000; Rauzi and Lenne, 2011; Samarage et al., 2015). We found minimal recoil in the ring before it reached the junctions, in regions distal from the advancing zipper, and in regions already zippered but treated with the ROCK inhibitor H-1152 (Figures 6D, 6E, and S6A–S6C). By contrast, ablation at the ring proximal to the advancing zipper and in rings already zippered along the junction resulted in marked recoil (Figures 6D and 6E), consistent with increased myosin II-mediated line tension in these regions (Figures 5D, 5E, and 5H).

We then disrupted myosin II activity in a time-restricted manner following ring formation but before zippering using the myosin II inhibitor blebbistatin or H-1152. The rings of these embryos failed to couple and zipper (Figures 6F–6H). Moreover, applying H-1152 immediately after the initial contact formed between two rings uncoupled the rings and reduced E-cad-GFP and GFP-ZO1 at that site (Figure S6D). Finally, applying H-1152 in embryos in which actin rings were already zippering halted the zippering process and triggered unzipping (Figure S6D). These results confirm that actin ring capture, coupling, and zippering all require myosin II-dependent tension.

Actin Ring Zippering Is Required to Seal the Embryo for Blastocyst Formation

We finally examined whether actin ring zippering is required to seal the embryo for blastocyst formation. Establishment of selective permeability barriers requires maturation of cell-cell junctions (Watson and Barcroft, 2001; Zihni et al., 2016). In line with this, fluorescence recovery after photobleaching (FRAP)

experiments demonstrated a larger immobile pool of E-cad-GFP (Figure 7A) and GFP- α -cat (Figure 7B) at zippered junctions compared to non-zippered junctions. Live imaging revealed the recruitment of ZO1, Occludin, and PLEKHA7 to the junctions (Figures 5C, 6B, S6E, and S6F), consistent with the idea that zippering triggers junctional maturation. Moreover, FDAP experiments demonstrated slower turnover and a larger immobile fraction of paGFP-actin at zippered compared to non-zippered junctions (Figure S6G).

To probe the requirement of zippering for embryo sealing, we monitored the diffusion of a fluorescently labeled dextran (dextran-fluorescein isothiocyanate [FITC]) throughout the intercellular spaces of the embryo (Moriwaki et al., 2007). Incubating embryos in dextran-FITC prior to zippering caused diffusion of dextran-FITC into the intercellular spaces (Figure 7C). Following zippering, embryos retained dextran-FITC until blastocyst stage when transferred to a saline solution, indicating successful sealing (Figure 7D). By contrast, both sealing and blastocyst formation were abolished by (1) disruption of actin rings using Pard6b downregulation, previously shown to affect cortical actin and tight junction assembly (Alarcon, 2010); (2) disruption of ring coupling to junctions using α -cat siRNAs; (3) prevention of zippering using blebbistatin and H-1152 in a time-restricted manner; and (4) disruption of tight junction formation via ZO1 knockdown (Figures 7D–7F and S6H–S6J). Therefore, actin ring formation and zippering is required for embryo sealing and the transition to blastocyst stage.

DISCUSSION

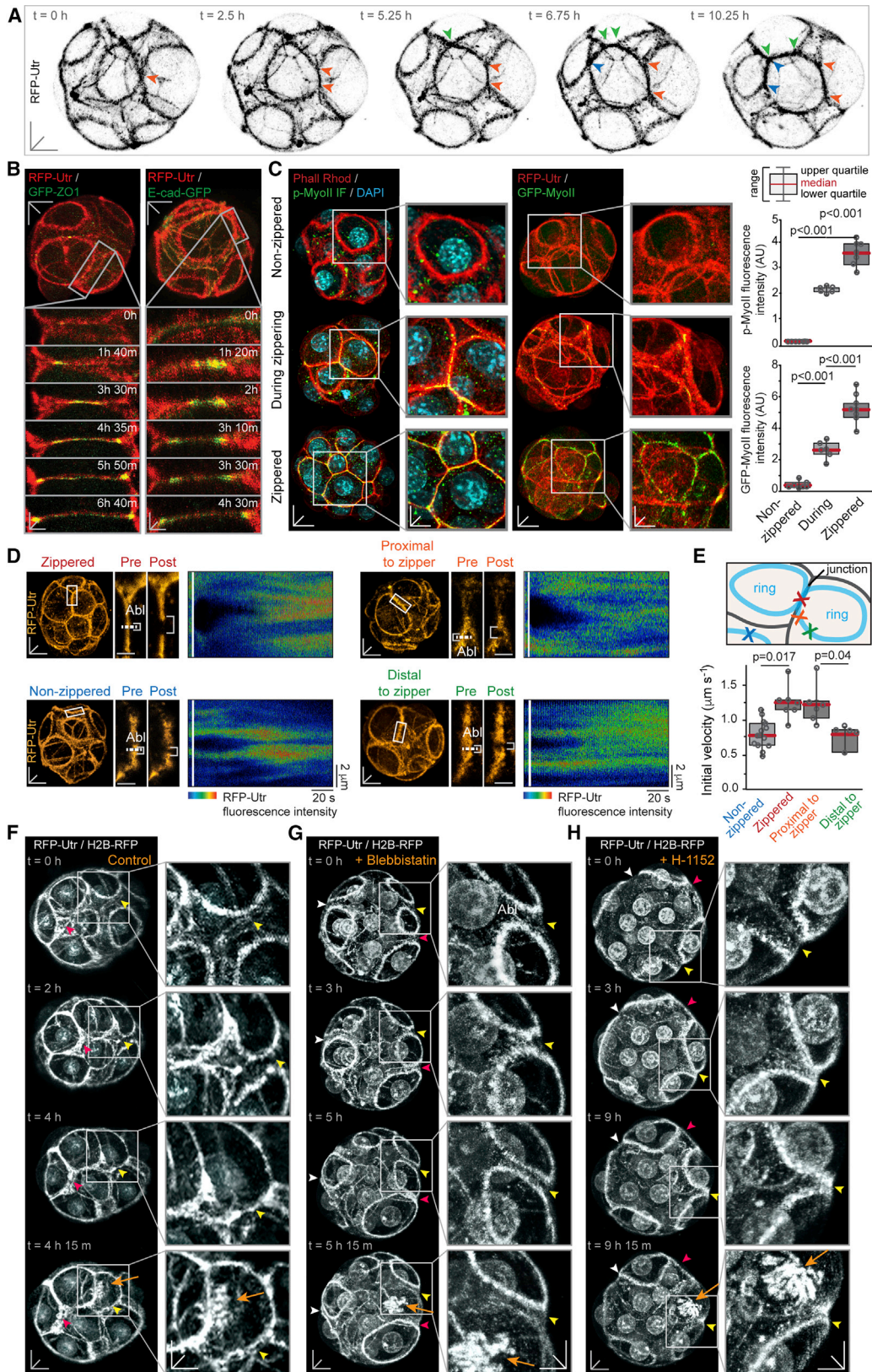
We reveal a coordinated morphogenetic mechanism that triggers sealing of the mouse embryo for blastocyst formation (Figure 7G). This mechanism comprises the following: (1) *de novo* formation of cortical F-actin rings, (2) expansion of the actin rings and coupling to the cell-cell junctions, and (3) zippering of actin rings along the junctions to trigger maturation of junctional complexes and seal the embryo.

Actin Ring Formation and Expansion

Although it is commonly assumed that apical domains established at the 8-cell stage are asymmetrically inherited during

Figure 5. Expanded Actin Rings Couple to Cell-Cell Junctions

(A–C) Coupled rings in 16-cell embryos co-localize with E-cad, α -cat, and ZO1 at junctions. Expanded actin rings in fixed embryos stained for E-cad (A), α -cat (B), or ZO1 (C) with Phalloidin-Rhodamine and DAPI (top panels) and in live embryos expressing RFP-Utr with E-cad-GFP, GFP- α -cat, or GFP-ZO1 (lower panels). Arrowheads indicate junctions without contact with rings (white, non-zippered), with one coupled actin ring (blue), or two coupled rings (magenta, zippered). (D) Live imaging shows recruitment of GFP-MyoII to the initial site of contact between the actin ring and the junction (arrowheads as in C). (E) GFP-MyoII intensity increases at the initial contact site between the actin ring and the junction and in proximal regions along the ring. (F) Live 16-cell embryos expressing RFP-Utr, H2B-RFP with E-cad- Δ ICD-GFP, or microinjected with α -cat or ZO1 siRNAs. The actin rings expand but do not couple to the junctions (arrowheads). Arrows indicate cell division at the end of the 16-cell stage. (G) E-cad- Δ ICD-GFP or siRNAs for α -cat or ZO1 delay actin ring expansion. (H) GFP-MyoII is progressively recruited as ring zippering proceeds along the junction. (I) Arrowheads indicate the junction before the first ring couples (blue), after the first ring couples (blue), and after the second ring couples (magenta). Arrows indicate a local deformation of the second ring at the region near the junction. (J) Schematic depicting how neighboring actin rings meet at the same initial contact site, not different sites along the junction. (K) Spatiotemporally controlled disruption of myosin II using azido-blebbistatin activation interferes with coupling of the second ring to the junction (n = 5 embryos). (L) Laser ablation (Ab) at the cortex between the second ring and the junction causes the ring to retract. Boxplots show median (red line), upper and lower quartiles, and range. Data in (A)–(C), (E), and (G) are presented as mean \pm SEM. Scale bars, 10 μ m in all images except for insets in (A)–(C) and (H), 3 μ m, and (I), (K), and (L), 5 μ m. n = junctions in (A)–(C), rings in (E) and (G), and embryos in (F).



(legend on next page)

division to regulate cell fate (Chazaud et al., 2006; Hirate et al., 2015; Leung et al., 2016; Maître et al., 2016; Yamanaka et al., 2006), direct imaging of this process in live embryos is lacking. We show that most actin rings are not inherited but form *de novo* in 16-cell-stage blastomeres via the action of cortical flows and a network of polar microtubules. Unlike well-described actin flows at the onset of cytokinesis directed toward the cytokinetic furrow (Reymann et al., 2016), the flow that forms the actin ring occurs following cytokinesis, likely due to disassembly of the actomyosin furrow (Montembault et al., 2017), and is directed away from the nascent junction toward the cell poles.

In dividing cells, astral microtubules originate from mitotic spindle centrosomes (Bettencourt-Dias and Glover, 2007). Consistent with the lack of centrosomes during early mouse development, we find no clear astral microtubules during mitosis in the early mouse embryo. However, a polar microtubule network emerges rapidly after telophase and excludes F-actin from the apical cortex, in a manner analogous to polar relaxation in other systems (Fededa and Gerlich, 2012; White and Borisy, 1983; Wolpert, 1960). Currently, the molecular basis of polar relaxation remains unclear. The disruption of actin rings resulting from Pard6b downregulation suggests that Par-aPKC complexes may be involved in clearing cortical F-actin, as demonstrated in numerous developmental processes (Alarcon, 2010; David et al., 2010; Munro et al., 2004; Zhu et al., 2017). We do not exclude the possibility that microtubule-independent mechanisms may also contribute to F-actin exclusion from the cortex. However, we propose that cortical actin flow and an inhibitory network of polar microtubules act in combination to form the actin ring in the region where the flow encounters these microtubules.

Although actin rings drive various morphogenetic events, they typically do so by constriction. Classical examples include the cytokinetic furrow driving cell division and concentric F-actin structures mediating wound healing (Schwayer et al., 2016). These rings accumulate myosin II and are contractile. Although a previous study detected myosin II at the apical cortex of the early mouse embryo (Maître et al., 2016), we find that the levels of GFP-MyoII in live embryos, and those of endogenous phospho-myosin II in fixed embryos, at the actin ring are negligible compared to those measured at the cytokinetic furrow or at junctions during zippering. Consistent with low myosin II levels, the actin ring is not contractile but instead expands over time, suggesting that myosin II-excluding mechanisms may operate at the actin ring.

The membrane bulge within the actin ring is morphologically similar to a cellular bleb, and the aperture delineated by the ring is comparable to the bleb neck. Hydrostatic forces acting on blebs

during expansion dissipate by increasing both bleb height and the radius of the aperture formed by the bleb neck (Tinevez et al., 2009). During division, contraction of one cell pole leads to the expansion of the opposite pole and formation of blebs. These blebs act as pressure sinks, buffering expansive forces directed at the cortex (Sedzinski et al., 2011). Analogously, in the cells of the embryo, apically directed hydrostatic forces arising from narrowing of their basolateral region after division should tend to inflate the bulge and expand its aperture and, consequently, the ring. Forces opposing expansion determine the extent to which either of these changes occurs. Membrane tension opposes expansion within the bulge and could be significant following its inflation, whereas contractility, crosslinking, and membrane anchoring oppose ring expansion. We have shown that the actin ring is not significantly contractile. Although the actin rings are enriched in the actin-bundling protein Fascin, we propose that, over the relatively long timescales of their expansion, any elastic effects resulting from actin bundling and crosslinking will not dominate forces opposing expansion. Our Ezrin manipulations instead indicate that friction originating from actin ring linkage to the plasma membrane is a dominant force opposing expansion.

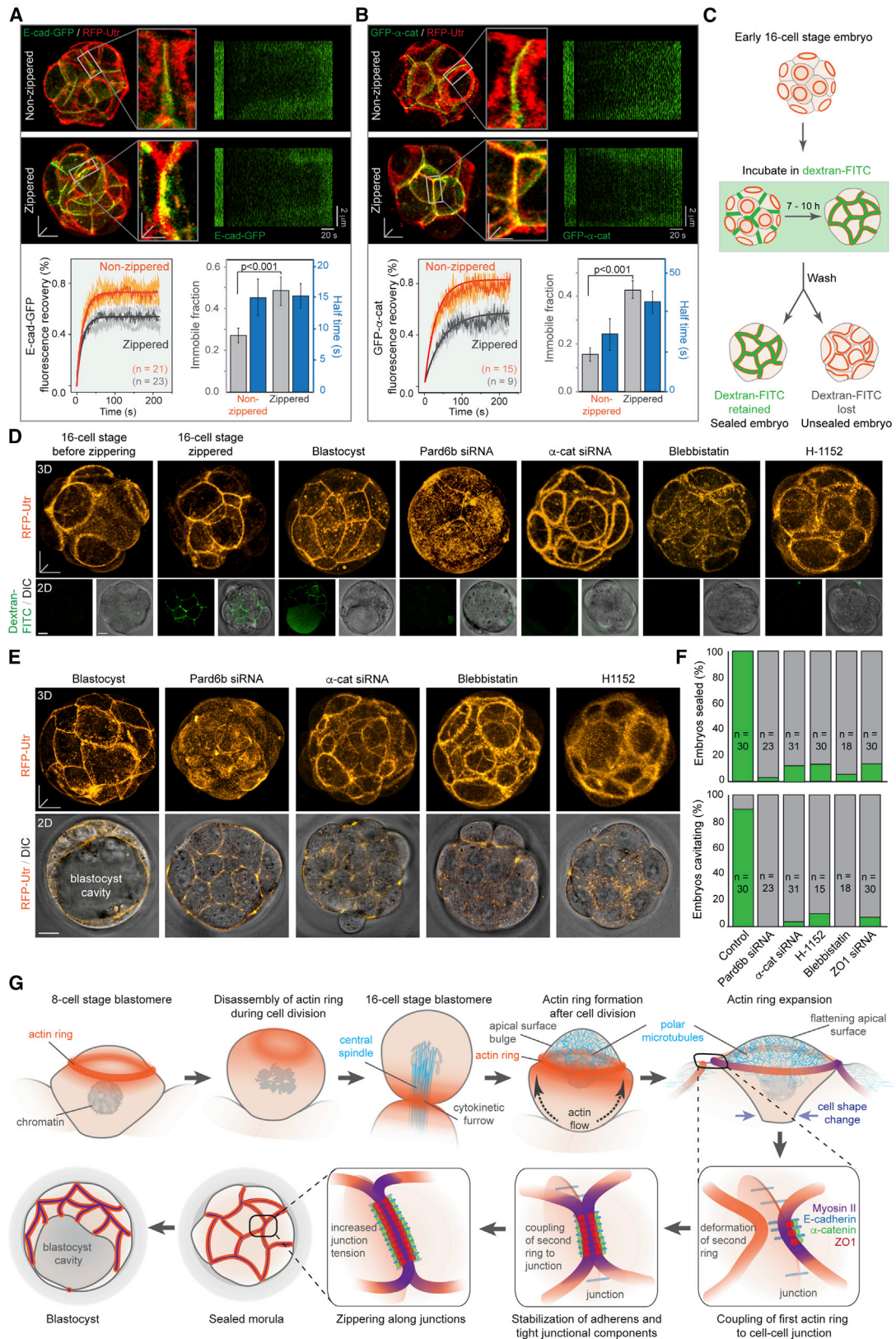
Actin ring expansion ultimately remodels most of the apical surface of the embryo, by replacing the F-actin cortex with a microtubule network. It will be interesting to explore whether the microtubule network physically displaces F-actin or interacts with the plasma membrane to reinforce the cortex in place of F-actin or to locally alter plasma membrane composition (Wolff, 2009). Actin ring expansion may also contribute to smoothening and flattening the apical surface of the embryo, thereby minimizing its surface energy and decreasing the exposed area that must be sealed for blastocyst formation. Furthermore, ring expansion may enable the delivery of proteins such as Occludin to the junctions, which could coordinate the timing of junctional maturation within the embryo.

Actin Ring Zippering and Embryo Sealing

The zippering of actin rings in the mouse embryo has similarities to the zippering described during dorsal closure in *Drosophila* (Choi et al., 2011; Kiehart et al., 2000) or chordate neurulation (Galea et al., 2017; Hashimoto et al., 2015), including the formation of a supracellular actin cable that enriches junctional components and promotes directional zippering of cells in a tension-dependent manner. However, whereas zippering in other systems involves large-scale multicellular movements to unite separate epithelial sheets, the rings of the mouse embryo form in cells that are already in contact and share a junction, and zippering occurs to mature and stabilize these junctions.

Figure 6. Actin Rings Undergo Tension-Dependent Zippering along the Cell-Cell Junctions

- (A) Zippering starts at the initial contact site between neighboring rings and progresses bidirectionally along junctions (arrowheads).
 (B) Zippering recruits and distributes E-cad-GFP and GFP-ZO1 along junctions.
 (C) Live and fixed embryos show increased myosin II at rings as they couple and zipper.
 (D) Laser ablations (Abl) demonstrate stronger recoil responses at the zippered region and proximal to the advancing zipper compared to ablations distal to the zippered region or to non-zippered regions.
 (E) Schematic illustration of ablation sites in (D) and graph of initial recoil velocity post-ablation.
 (F) Control embryos zipper during the 16-cell stage. Arrowheads indicate junctions with proximal rings. Orange arrows indicate when the cell enters division at the end of the 16-cell stage.
 (G and H) Blebbistatin (G) or H-1152 (H) prevents zippering.
 Data in (C) and (E) are presented as mean \pm SEM. Scale bars, 10 μ m in all images except for insets in (B) and (D), 3 μ m, and insets in (C), 5 μ m; n = rings or junctions.



(legend on next page)

In contrast to actin ring expansion, zippering is myosin II and tension dependent. The initial accumulation of myosin II occurs when the first ring couples to the junction. This localized myosin II enrichment increases tension at the junction, which likely recruits myosin II to the opposite side of the junction within the neighboring cell (Kim et al., 2015; Yap et al., 2017). This feedback mode of regulation, in which tension can enhance the recruitment of myosin II, coordinates multicellular actomyosin cables in *Drosophila* embryos (Fernandez-Gonzalez et al., 2009). The accumulation of myosin II and increase in tension along the ring proximal to the junctional contact site may contribute to the net force driving advancement of the zipper along the junction. Once zippering is complete, myosin II remains enriched along the apical junctions, where it could contribute to junctional stability (Arnold et al., 2017) and mechanochemical feedback (Yap et al., 2017).

It is rare for a single actin ring to zipper along the length of the junction alone (i.e., without a neighboring ring zippering along the other side of the junction). Moreover, we do not observe establishment of multiple zippering points at the same junction by two neighboring rings. Therefore, the ability of the first actin ring to capture its neighboring ring to the same site may increase the fidelity of embryo sealing. Zippering proceeds along the junction to tricellular junctions, consistent with reports that vertices provide physical barriers to lateral displacement of actin bundles and junctional components and serve as specialized sites of actomyosin attachment to the cortex (Cavey et al., 2008; Rauzi et al., 2008).

Finally, we demonstrate that actin ring zippering coordinates the assembly and maturation of adherens and tight junction components, which are required to seal the embryo and withstand the increase in internal pressure during cavitation. Consistent with other systems, the increase in tension along zippered junctions is accompanied by stabilization of actin and junctional components (Priya et al., 2013; Smutny et al., 2010; Yonemura et al., 2010). The progression of actin ring zippering along the junctions transforms them from primordial junctions into a mature junctional belt (Yonemura et al., 1995). We propose that establishment and retention of this zippered architecture during cell divisions after the 16-cell stage maintains the permeability barrier, thereby enabling successful completion of blastocyst formation.

STAR★METHODS

Detailed methods are provided in the online version of this paper and include the following:

- KEY RESOURCES TABLE
- CONTACT FOR REAGENT AND RESOURCE SHARING

- EXPERIMENTAL MODEL AND SUBJECT DETAILS
- METHOD DETAILS
 - Mouse embryo work
 - Live embryo imaging
- QUANTIFICATION AND STATISTICAL ANALYSIS
 - Image analysis
 - EB3-dTomato tracking
 - Curvature analysis
 - FDAP analysis
 - FRAP analysis
 - Laser ablation analysis
 - PIV analysis
 - Statistical analysis

SUPPLEMENTAL INFORMATION

Supplemental Information includes six figures and eight movies and can be found with this article online at <https://doi.org/10.1016/j.cell.2018.02.035>.

ACKNOWLEDGMENTS

This work was supported by funds from the DFG (ZE997/1-1), SNF (PBLAP3-145877), and HFSP (LT000164/2015) to J.Z.; EMBL Australia to M.B.; and A*STAR (2013APP005), EMBO, and HHMI-Wellcome Trust to N.P. H.Y.G.L. is a member of the Graduate School for Integrative Sciences and Engineering, NUS. We thank O. Thorn-Seshold, M. Govendir, A. Masedunskas, P. Gunning, R. Zaidel-Bar, O. Campas, and O. Hamant for sharing reagents and advice.

AUTHOR CONTRIBUTIONS

J.Z., M.D.W., M.G., Y.D.A., H.Y.G.L., and S.B. performed experiments and data analysis. All authors contributed to writing the paper.

DECLARATION OF INTERESTS

The authors declare no competing interests.

Received: October 2, 2017
 Revised: December 20, 2017
 Accepted: February 15, 2018
 Published: March 22, 2018

REFERENCES

- Alarcon, V.B. (2010). Cell polarity regulator PARD6B is essential for trophectoderm formation in the preimplantation mouse embryo. *Biol. Reprod.* **83**, 347–358.
- Anani, S., Bhat, S., Honma-Yamanaka, N., Krawchuk, D., and Yamanaka, Y. (2014). Initiation of Hippo signaling is linked to polarity rather than to cell position in the pre-implantation mouse embryo. *Development* **141**, 2813–2824.
- Arnold, T.R., Stephenson, R.E., and Miller, A.L. (2017). Rho GTPases and actomyosin: Partners in regulating epithelial cell-cell junction structure and function. *Exp. Cell Res.* **358**, 20–30.

Figure 7. Actin Zippering Seals the Embryo for Blastocyst Formation

(A and B) FRAP demonstrates a larger immobile fraction of E-cad-GFP (A) and GFP- α -cat (B) at zippered junctions.

(C) Permeability assay for embryo sealing. The dextran-FITC is lost if the sealing process is disrupted.

(D) Dextran-FITC is lost from live embryos following downregulation of Pard6b or α -catenin using siRNAs or treatment with blebbistatin or H-1152.

(E and F) Disrupting ring formation and zippering prevents blastocyst formation (E) and embryo sealing (F).

(G) Schematic summary of events driving ring formation, expansion, and zippering.

Data in (A) and (B) are presented as mean \pm SEM. Scale bars, 10 μ m in all images except for insets in (A) and (B), 3 μ m; n = junctions in (A) and (B) and embryos in (F).

- Arora, R., Fries, A., Oelrich, K., Marchuk, K., Sabeur, K., Giudice, L.C., and Laird, D.J. (2016). Insights from imaging the implanting embryo and the uterine environment in three dimensions. *Development* **143**, 4749–4754.
- Bettencourt-Dias, M., and Glover, D.M. (2007). Centrosome biogenesis and function: centrosomes brings new understanding. *Nat. Rev. Mol. Cell Biol.* **8**, 451–463.
- Biro, M., Romeo, Y., Kroschwald, S., Bovellan, M., Boden, A., Tcherkezian, J., Roux, P.P., Charras, G., and Paluch, E.K. (2013). Cell cortex composition and homeostasis resolved by integrating proteomics and quantitative imaging. *Cytoskeleton (Hoboken)* **70**, 741–754.
- Borowiak, M., Nahaboo, W., Reynders, M., Nekolla, K., Jalinet, P., Hasserodt, J., Rehberg, M., Delattre, M., Zahler, S., Vollmar, A., et al. (2015). Photoswitchable Inhibitors of Microtubule Dynamics Optically Control Mitosis and Cell Death. *Cell* **162**, 403–411.
- Burkel, B.M., von Dassow, G., and Bement, W.M. (2007). Versatile fluorescent probes for actin filaments based on the actin-binding domain of utrophin. *Cell Motil. Cytoskeleton* **64**, 822–832.
- Canman, J.C., and Bement, W.M. (1997). Microtubules suppress actomyosin-based cortical flow in *Xenopus* oocytes. *J. Cell Sci.* **110**, 1907–1917.
- Cassimeris, L., Guglielmi, L., Denis, V., Larroque, C., and Martineau, P. (2013). Specific *in vivo* labeling of tyrosinated α -tubulin and measurement of microtubule dynamics using a GFP tagged, cytoplasmically expressed recombinant antibody. *PLoS ONE* **8**, e59812.
- Cavey, M., Rauzi, M., Lenne, P.F., and Lecuit, T. (2008). A two-tiered mechanism for stabilization and immobilization of E-cadherin. *Nature* **453**, 751–756.
- Charras, G., and Paluch, E. (2008). Blebs lead the way: how to migrate without lamellipodia. *Nat. Rev. Mol. Cell Biol.* **9**, 730–736.
- Chazaud, C., Yamanaka, Y., Pawson, T., and Rossant, J. (2006). Early lineage segregation between epiblast and primitive endoderm in mouse blastocysts through the Grb2-MAPK pathway. *Dev. Cell* **10**, 615–624.
- Choi, W., Jung, K.C., Nelson, K.S., Bhat, M.A., Beitel, G.J., Peifer, M., and Fanning, A.S. (2011). The single *Drosophila* ZO-1 protein Polychaetoid regulates embryonic morphogenesis in coordination with Cnca/afadin and Enabled. *Mol. Biol. Cell* **22**, 2010–2030.
- Clift, D., and Schuh, M. (2015). A three-step MTOC fragmentation mechanism facilitates bipolar spindle assembly in mouse oocytes. *Nat. Commun.* **6**, 7217.
- Coelho, P.A., Bury, L., Sharif, B., Riparbelli, M.G., Fu, J., Callaini, G., Glover, D.M., and Zernicka-Goetz, M. (2013). Spindle formation in the mouse embryo requires Plk4 in the absence of centrioles. *Dev. Cell* **27**, 586–597.
- Conduit, P.T., Wainman, A., and Raff, J.W. (2015). Centrosome function and assembly in animal cells. *Nat. Rev. Mol. Cell Biol.* **16**, 611–624.
- Dard, N., Louvet, S., Santa-Maria, A., Aghion, J., Martin, M., Mangeat, P., and Maro, B. (2001). *In vivo* functional analysis of ezrin during mouse blastocyst formation. *Dev. Biol.* **233**, 161–173.
- David, D.J., Tishkina, A., and Harris, T.J. (2010). The PAR complex regulates pulsed actomyosin contractions during amnioserosa apical constriction in *Drosophila*. *Development* **137**, 1645–1655.
- Diz-Muñoz, A., Krieg, M., Bergert, M., Ibarlucea-Benitez, I., Muller, D.J., Paluch, E., and Heisenberg, C.P. (2010). Control of directed cell migration *in vivo* by membrane-to-cortex attachment. *PLoS Biol.* **8**, e1000544.
- Ducibella, T., Albertini, D.F., Anderson, E., and Biggers, J.D. (1975). The pre-implantation mammalian embryo: characterization of intercellular junctions and their appearance during development. *Dev. Biol.* **45**, 231–250.
- Eckert, J.J., and Fleming, T.P. (2008). Tight junction biogenesis during early development. *Biochim. Biophys. Acta* **1778**, 717–728.
- Fanning, A.S., Van Itallie, C.M., and Anderson, J.M. (2012). Zonula occludens-1 and -2 regulate apical cell structure and the zonula adherens cytoskeleton in polarized epithelia. *Mol. Biol. Cell* **23**, 577–590.
- Fededa, J.P., and Gerlich, D.W. (2012). Molecular control of animal cell cytokinesis. *Nat. Cell Biol.* **14**, 440–447.
- Fernandez-Gonzalez, R., Simoes, Sde.M., Röper, J.C., Eaton, S., and Zallen, J.A. (2009). Myosin II dynamics are regulated by tension in intercalating cells. *Dev. Cell* **17**, 736–743.
- Fierro-González, J.C., White, M.D., Silva, J.C., and Plachta, N. (2013). Cadherin-dependent filopodia control preimplantation embryo compaction. *Nat. Cell Biol.* **15**, 1424–1433.
- Galea, G.L., Cho, Y.J., Galea, G., Molè, M.A., Rolo, A., Savery, D., Moulding, D., Culshaw, L.H., Nikolopoulou, E., Greene, N.D.E., and Copp, A.J. (2017). Biomechanical coupling facilitates spinal neural tube closure in mouse embryos. *Proc. Natl. Acad. Sci. USA* **114**, E5177–E5186.
- Hashimoto, H., Robin, F.B., Sherrard, K.M., and Munro, E.M. (2015). Sequential contraction and exchange of apical junctions drives zippering and neural tube closure in a simple chordate. *Dev. Cell* **32**, 241–255.
- Heisenberg, C.P., and Bellaïche, Y. (2013). Forces in tissue morphogenesis and patterning. *Cell* **153**, 948–962.
- Hirate, Y., Hirahara, S., Inoue, K., Kiyonari, H., Niwa, H., and Sasaki, H. (2015). Par-aPKC-dependent and -independent mechanisms cooperatively control cell polarity, Hippo signaling, and cell positioning in 16-cell stage mouse embryos. *Dev. Growth Differ.* **57**, 544–556.
- Howe, K., and FitzHarris, G. (2013). A non-canonical mode of microtubule organization operates throughout pre-implantation development in mouse. *Cell Cycle* **12**, 1616–1624.
- Johnson, M.H., and Maro, B. (1984). The distribution of cytoplasmic actin in mouse 8-cell blastomeres. *J. Embryol. Exp. Morphol.* **82**, 97–117.
- Kaur, G., Costa, M.W., Nefzger, C.M., Silva, J., Fierro-González, J.C., Polo, J.M., Bell, T.D., and Plachta, N. (2013). Probing transcription factor diffusion dynamics in the living mammalian embryo with photoactivatable fluorescence correlation spectroscopy. *Nat. Commun.* **4**, 1637.
- Képiró, M., Várkuti, B.H., Bodor, A., Hegyi, G., Drahos, L., Kovács, M., and Málnási-Csizmadia, A. (2012). Azidoblebbistatin, a photoreactive myosin inhibitor. *Proc. Natl. Acad. Sci. USA* **109**, 9402–9407.
- Kiehart, D.P., Galbraith, C.G., Edwards, K.A., Rickoll, W.L., and Montague, R.A. (2000). Multiple forces contribute to cell sheet morphogenesis for dorsal closure in *Drosophila*. *J. Cell Biol.* **149**, 471–490.
- Kim, J.H., Ren, Y., Ng, W.P., Li, S., Son, S., Kee, Y.S., Zhang, S., Zhang, G., Fletcher, D.A., Robinson, D.N., and Chen, E.H. (2015). Mechanical tension drives cell membrane fusion. *Dev. Cell* **32**, 561–573.
- Lecuit, T., and Yap, A.S. (2015). E-cadherin junctions as active mechanical integrators in tissue dynamics. *Nat. Cell Biol.* **17**, 533–539.
- Lecuit, T., Lenne, P.F., and Munro, E. (2011). Force generation, transmission, and integration during cell and tissue morphogenesis. *Annu. Rev. Cell Dev. Biol.* **27**, 157–184.
- Leung, C.Y., Zhu, M., and Zernicka-Goetz, M. (2016). Polarity in Cell-Fate Acquisition in the Early Mouse Embryo. *Curr. Top. Dev. Biol.* **120**, 203–234.
- Maiers, J.L., Peng, X., Fanning, A.S., and DeMali, K.A. (2013). ZO-1 recruitment to α -catenin—a novel mechanism for coupling the assembly of tight junctions to adherens junctions. *J. Cell Sci.* **126**, 3904–3915.
- Maître, J.L., Turlier, H., Illukkumbura, R., Eismann, B., Niwayama, R., Nédélec, F., and Hiragi, T. (2016). Asymmetric division of contractile domains couples cell positioning and fate specification. *Nature* **536**, 344–348.
- Mayer, M., Depken, M., Bois, J.S., Jülicher, F., and Grill, S.W. (2010). Anisotropies in cortical tension reveal the physical basis of polarizing cortical flows. *Nature* **467**, 617–621.
- McLaren, A., and Smith, R. (1977). Functional test of tight junctions in the mouse blastocyst. *Nature* **267**, 351–353.
- Meng, W., Mushika, Y., Ichii, T., and Takeichi, M. (2008). Anchorage of microtubule minus ends to adherens junctions regulates epithelial cell–cell contacts. *Cell* **135**, 948–959.
- Montebault, E., Claverie, M.C., Bouit, L., Landmann, C., Jenkins, J., Tsankova, A., Cabernard, C., and Royou, A. (2017). Myosin efflux promotes cell elongation to coordinate chromosome segregation with cell cleavage. *Nat. Commun.* **8**, 326.

- Moriwaki, K., Tsukita, S., and Furuse, M. (2007). Tight junctions containing claudin 4 and 6 are essential for blastocyst formation in preimplantation mouse embryos. *Dev. Biol.* *312*, 509–522.
- Morris, S.A., Teo, R.T., Li, H., Robson, P., Glover, D.M., and Zernicka-Goetz, M. (2010). Origin and formation of the first two distinct cell types of the inner cell mass in the mouse embryo. *Proc. Natl. Acad. Sci. USA* *107*, 6364–6369.
- Munro, E., Nance, J., and Priess, J.R. (2004). Cortical flows powered by asymmetrical contraction transport PAR proteins to establish and maintain anterior-posterior polarity in the early *C. elegans* embryo. *Dev. Cell* *7*, 413–424.
- Plachta, N., Bollenbach, T., Pease, S., Fraser, S.E., and Pantazis, P. (2011). Oct4 kinetics predict cell lineage patterning in the early mammalian embryo. *Nat. Cell Biol.* *13*, 117–123.
- Priya, R., Yap, A.S., and Gomez, G.A. (2013). E-cadherin supports steady-state Rho signaling at the epithelial zonula adherens. *Differentiation* *86*, 133–140.
- Rauzi, M., and Lenne, P.F. (2011). Cortical forces in cell shape changes and tissue morphogenesis. *Curr. Top. Dev. Biol.* *95*, 93–144.
- Rauzi, M., Verant, P., Lecuit, T., and Lenne, P.F. (2008). Nature and anisotropy of cortical forces orienting *Drosophila* tissue morphogenesis. *Nat. Cell Biol.* *10*, 1401–1410.
- Riedl, J., Crevenna, A.H., Kessenbrock, K., Yu, J.H., Neukirchen, D., Bista, M., Bradke, F., Jenne, D., Holak, T.A., and Werb, Z. (2008). Lifeact: a versatile marker to visualize F-actin. *Nat. Methods* *5*, 605–607.
- Reymann, A.C., Staniscia, F., Erzberger, A., Salbreux, G., and Grill, S.W. (2016). Cortical flow aligns actin filaments to form a furrow. *eLife* *5*, e17807.
- Samarage, C.R., White, M.D., Álvarez, Y.D., Fierro-González, J.C., Henon, Y., Jesudason, E.C., Bissiere, S., Fouras, A., and Plachta, N. (2015). Cortical Tension Allocates the First Inner Cells of the Mammalian Embryo. *Dev. Cell* *34*, 435–447.
- Schwayer, C., Sikora, M., Slovák, J., Kardos, R., and Heisenberg, C.P. (2016). Actin Rings of Power. *Dev. Cell* *37*, 493–506.
- Sedzinski, J., Biro, M., Oswald, A., Tinevez, J.Y., Salbreux, G., and Paluch, E. (2011). Polar actomyosin contractility destabilizes the position of the cytokinetic furrow. *Nature* *476*, 462–466.
- Smutny, M., Cox, H.L., Leerberg, J.M., Kovacs, E.M., Conti, M.A., Ferguson, C., Hamilton, N.A., Parton, R.G., Adelstein, R.S., and Yap, A.S. (2010). Myosin II isoforms identify distinct functional modules that support integrity of the epithelial zonula adherens. *Nat. Cell Biol.* *12*, 696–702.
- Stephenson, R.O., Yamanaka, Y., and Rossant, J. (2010). Disorganized epithelial polarity and excess trophectoderm cell fate in preimplantation embryos lacking E-cadherin. *Development* *137*, 3383–3391.
- Tinevez, J.Y., Schulze, U., Salbreux, G., Roensch, J., Joanny, J.F., and Paluch, E. (2009). Role of cortical tension in bleb growth. *Proc. Natl. Acad. Sci. USA* *106*, 18581–18586.
- Tornavaca, O., Chia, M., Dufton, N., Almagro, L.O., Conway, D.E., Randi, A.M., Schwartz, M.A., Matter, K., and Balda, M.S. (2015). ZO-1 controls endothelial adherens junctions, cell-cell tension, angiogenesis, and barrier formation. *J. Cell Biol.* *208*, 821–838.
- Van Itallie, C.M., Fanning, A.S., Bridges, A., and Anderson, J.M. (2009). ZO-1 stabilizes the tight junction solute barrier through coupling to the perijunctional cytoskeleton. *Mol. Biol. Cell* *20*, 3930–3940.
- Watanabe, T., Biggins, J.S., Tannan, N.B., and Srinivas, S. (2014). Limited predictive value of blastomere angle of division in trophectoderm and inner cell mass specification. *Development* *141*, 2279–2288.
- Watson, A.J., and Barcroft, L.C. (2001). Regulation of blastocyst formation. *Front. Biosci.* *6*, D708–D730.
- White, J.G., and Borisy, G.G. (1983). On the mechanisms of cytokinesis in animal cells. *J. Theor. Biol.* *101*, 289–316.
- White, M.D., Zenker, J., Bissiere, S., and Plachta, N. (2017). How cells change shape and position in the early mammalian embryo. *Curr. Opin. Cell Biol.* *44*, 7–13.
- Wolff, J. (2009). Plasma membrane tubulin. *Biochim. Biophys. Acta* *1788*, 1415–1433.
- Wolpert, L. (1960). The mechanics and mechanism of cleavage. *Int. Rev. Cytol.* *10*, 163–216.
- Yamanaka, Y., Ralston, A., Stephenson, R.O., and Rossant, J. (2006). Cell and molecular regulation of the mouse blastocyst. *Dev. Dyn.* *235*, 2301–2314.
- Yamanaka, Y., Lanner, F., and Rossant, J. (2010). FGF signal-dependent segregation of primitive endoderm and epiblast in the mouse blastocyst. *Development* *137*, 715–724.
- Yamashita, N., Morita, M., Legant, W.R., Chen, B.C., Betzig, E., Yokota, H., and Mimori-Kiyosue, Y. (2015). Three-dimensional tracking of plus-tips by lattice light-sheet microscopy permits the quantification of microtubule growth trajectories within the mitotic apparatus. *J. Biomed. Opt.* *20*, 101206.
- Yap, A.S., Duszyc, K., and Viasnoff, V. (2017). Mechanosensing and Mechanotransduction at Cell-Cell Junctions. *Cold Spring Harb. Perspect. Biol.* Published online August 4, 2017. <https://doi.org/10.1101/cshperspect.a028761>.
- Yonemura, S., Itoh, M., Nagafuchi, A., and Tsukita, S. (1995). Cell-to-cell adherens junction formation and actin filament organization: similarities and differences between non-polarized fibroblasts and polarized epithelial cells. *J. Cell Sci.* *108*, 127–142.
- Yonemura, S., Wada, Y., Watanabe, T., Nagafuchi, A., and Shibata, M. (2010). alpha-Catenin as a tension transducer that induces adherens junction development. *Nat. Cell Biol.* *12*, 533–542.
- Zenker, J., White, M.D., Templin, R.M., Parton, R.G., Thorn-Seshold, O., Bissiere, S., and Plachta, N. (2017). A microtubule-organizing center directing intracellular transport in the early mouse embryo. *Science* *357*, 925–928.
- Zhu, M., Leung, C.Y., Shahbazi, M.N., and Zernicka-Goetz, M. (2017). Actomyosin polarisation through PLC-PKC triggers symmetry breaking of the mouse embryo. *Nat. Commun.* *8*, 921.
- Zihni, C., Mills, C., Matter, K., and Balda, M.S. (2016). Tight junctions: from simple barriers to multifunctional molecular gates. *Nat. Rev. Mol. Cell Biol.* *17*, 564–580.

STAR★METHODS

KEY RESOURCES TABLE

REAGENT or RESOURCE	SOURCE	IDENTIFIER
Antibodies		
Phospho-Ezrin (T567)/Radixin (564)/Moesin (T558), Rabbit polyclonal	Cell Signaling Technology	3149
Phospho-Myosin Light Chain 2 (S19), Rabbit polyclonal	Cell Signaling Technology	3671
ZO1, Mouse monoclonal	Invitrogen	33-9100
Anti-Rabbit-Alexa 488, Donkey polyclonal	Invitrogen	A21206
Anti-Mouse-Alexa 488, Donkey polyclonal	Invitrogen	A21202
Anti-Rat-Alexa 488, Goat polyclonal	Invitrogen	A11006
α -catenin, Rabbit polyclonal	Sigma	C2081
α -tubulin, Mouse monoclonal	Sigma	T6199
DECMA1, Rat monoclonal	Sigma	U3254
IgG control antibody	Sigma	M5284
Chemicals, Peptides, and Recombinant Proteins		
Azido-blebbistatin	Opto-Pharma	N/A
H-1152	Tocris	2414
PST-1P	(Borowiak et al., 2015)	N/A
KSOM+AA	Merck	MR-020P-5F
PMS Pregnant Mare Serum Gonadotropin	National Hormone and Peptide Program	http://www.humc.edu
Recombinant Chorionic Gonadotropin CG	National Hormone and Peptide Program	http://www.humc.edu
Phalloidin-Rhodamine	Molecular Probes	R415
Blebbistatin	Sigma	B0560
CK-666	Sigma	SML0006
DAPI	Sigma	10236276001
Fluorescein isothiocyanate-dextran 40kD	Sigma	FD40
Nocodazole	Sigma	M1404
M2 medium	Sigma	M7167-100ML
Mineral oil	Sigma	M5310-1L
SMIFH2	Sigma	S4826
Rhodamine Wheat Germ Agglutinin	Vector Laboratories	RL-1022
Critical Commercial Assays		
mMESSAGE mMACHINE SP6 kit	ThermoFisher Sci	AM1340
RNeasy mini kit	QIAGEN	74106
Experimental Models: Organisms/Strains		
FVB/N mice	A*STAR	N/A
C57BL/6 mice	A*STAR	N/A
B6CBA-F1 mice	A*STAR	N/A
Oligonucleotides		
siRNA targeting sequence: E-cad Cdh1 #5: ACGGAGGAGAACGGTGGTCAA	QIAGEN	SI02711779
siRNA targeting sequence: E-cad Cdh1 #6: CCGGGACAATGTGTATTACTA	QIAGEN	SI02736146
siRNA targeting sequence: α -catenin Catna1 #1: CAGATGGAATTAATGACCAA	QIAGEN	SI00187852

(Continued on next page)

Continued

REAGENT or RESOURCE	SOURCE	IDENTIFIER
siRNA targeting sequence: α -catenin Catna1 #6: CTGGTAAACACCAATAGTAAA	QIAGEN	SI02711688
siRNA targeting sequence: Myosin II Myh9 #1: CAGGGCTTATCTACACCTATT	QIAGEN	SI01321411
siRNA targeting sequence: Myosin II Myh9 #3: TCCAGCAAGAATGGCTTTGAA	QIAGEN	SI01321425
siRNA targeting sequence: ZO1 Tjp1 #6: TAGG AGATTCATTCTATATTA	QIAGEN	SI02688896
siRNA targeting sequence: ZO1 Tjp1 #8: CTGA ATCTATAAATTAACATA	QIAGEN	SI02735236
siRNA targeting sequence: Ezrin Vil2 #4: CCAG TTTAAATTCCGGGCCAA	QIAGEN	SI00185437
siRNA targeting sequence: Ezrin Vil2 #5: GAGG ATAGTATTTATATATAA	QIAGEN	SI02669163
AllStars negative control siRNA: Sequence undisclosed by QIAGEN	QIAGEN	SI03650318
Recombinant DNA		
GFP-MAP2c	Michel Bornens	N/A
RFP-MAP2c	Michel Bornens	N/A
GFP-UtrCH	Addgene	26737
RFP-UtrCH	Addgene	26739
H2B-GFP	This study	N/A
H2B-RFP	Addgene	53745
GFP-actin	James Nelson	N/A
paGFP-actin	James Nelson	N/A
GFP-Pard6b	(Alarcon, 2010)	N/A
EB3-dTomato	Addgene	50708
E-cad-GFP	Alpha Yap	N/A
E-cad Δ ICD-GFP	(Samarage et al., 2015)	N/A
GFP- α -catenin	Addgene	20139
GFP-MyoII	Addgene	11347
GFP-ZO1	Addgene	30313
Ezrin-GFP	Addgene	20680
Ezrin-mRuby2	This study	N/A
PLEKHA7-GFP	(Meng et al., 2008)	N/A
2G4-GFP	(Cassimeris et al., 2013)	N/A
Occludin-Emerald	Addgene	54212
Lck-GFP	Addgene	61099
Lifeact-GFP	(Riedl et al., 2008)	N/A
Emerald-Fascin	Addgene	54094
Software and Algorithms		
ImageJ	N/A	https://imagej.nih.gov/ij/
Imaris 8.2	Bitplane	http://www.bitplane.com/imaris
MATLAB	Mathworks	https://www.mathworks.com/
Prism	GraphPad	https://www.graphpad.com/
ZEN	Zeiss	https://www.zeiss.com/microscopy/int/products/microscope-software/zen-lite.html
Other		
LabTek chambers	Thermo Fisher Scientific	155411

CONTACT FOR REAGENT AND RESOURCE SHARING

Further information and requests for resources and reagents should be directed to and will be fulfilled by the Lead Contact N.P.: plachtan@imcb.a-star.edu.sg

EXPERIMENTAL MODEL AND SUBJECT DETAILS

Superovulated C57BL/6 and FVB/N wild-type female mice were used following animal ethics guidelines of the Agency for Science, Technology and Research (Singapore). Superovulation regime consisted of 5 iu of pregnant mare serum (PMS, National Hormone and Peptide Program) gonadotropin given intraperitoneally and 5 iu of recombinant chorionic gonadotrophin (CG, National Hormone and Peptide Program), given 48 h later, immediately before mating. Embryos were flushed from oviducts with M2 medium (Merck) and cultured in KSOM+AA (Merck) at 37°C and 5% CO₂ covered by mineral oil (Sigma).

METHOD DETAILS

Mouse embryo work

Embryos were microinjected with 0.1 to 0.3 pL RNA diluted in injection buffer (5 mM Tris, 5 mM NaCl, 0.1 mM EDTA) with a FemtoJet (Eppendorf). For imaging, embryos were cultured in LabTek chambers (Nunc) at 37°C and 5% CO₂ in an incubator adapted for the microscope system (Carl Zeiss, Jena). All DNA constructs have been cloned into pCS2+ vector for RNA production. The mMACHINE mMACHINE® SP6 kit (Ambion) was used to synthesize RNA using linearized plasmids as templates following manufacturer's instructions. RNA was purified using RNAeasy kit (QIAGEN) following manufacturer's instructions. Embryos were microinjected with the following RNAs: paGFP-actin, GFP-Pard6b, EB3-dTomato GFP-actin, GFP-ZO1, Occludin-Emerald, aPKC-Emerald, Emerald-Fascin at 100 ng μl^{-1} ; GFP-MAP2c/RFP-MAP2c, PLEKHA7-GFP at 80 ng μl^{-1} ; 2G4-GFP, GFP-Utr, RFP-Utr at 75 ng μl^{-1} ; E-cad-GFP at 70 ng μl^{-1} ; GFP-MyoII, Lck-GFP, GFP- α -cat, Lifeact-GFP at 60 ng μl^{-1} ; H2B-RFP, H2B-GFP at 5 ng μl^{-1} ; Ezrin-GFP or Ezrin-mRuby at 50 ng μl^{-1} or 200 ng μl^{-1} for overexpression experiments and E-cad- Δ ICD-GFP at 200 ng μl^{-1} . Embryos showing signs of abnormal or arrested development (~15%) were excluded following established criteria (Fierro-González et al., 2013; Kaur et al., 2013; Morris et al., 2010). We previously demonstrated that embryos microinjected and imaged with similar conditions can generate viable offspring following transfer to pseudopregnant mice (Kaur et al., 2013).

siRNAs (QIAGEN) were microinjected at 200 nM.

Myosin II inhibition was performed with blebbistatin (Sigma, B0560), azido-blebbistatin (Opto-pharma) or ROCK inhibitor H-1152 (TOCRIS, 2414) at 50 μM in KSOM+AA. For microtubules disruption nocodazole (Sigma, M1404) was used at 10 μM in KSOM+AA for 15 m, 90 m or 9 h. PST-1P was used at 40 μM in KSOM+AA; embryos were incubated for 24 h in the dark before the experiment. Pan-Formin inhibition was performed with SMIFH2 (Sigma, S4826) at 250 μM in KSOM+AA. Arp2/3 inhibition was done using CK-666 (Sigma, SML0006) at 250 μM in KSOM+AA. For disruption of cortical flows in a time-restricted manner, embryos were monitored using live imaging to identify cells undergoing division. WGA (Vector Laboratories, RL-1022) was then applied at 100 $\mu\text{g ml}^{-1}$ and the newly divided cells were imaged with higher spatio-temporal resolution and using with PIV.

For immunolabeling, embryos were fixed in 4% paraformaldehyde in DPBS for 30 m at room temperature, washed in DPBS containing 0.1% Triton X-100, permeabilized for 30 m in DPBS containing 0.25% Triton X-100, incubated in blocking solution (10% fetal bovine serum in DPBS) for 2 h, incubated with antibodies for: phospho-Ezrin (Cell Signaling Technology) at 1:200, phospho-Myosin Light Chain 2 (Cell Signaling Technology, 3671P) at 1:200, ZO1 (Invitrogen, 33-9100) at 1:200, E-cad DECMA-1 (Sigma, U3254) at 1:100, α -catenin (Sigma, C2081) at 1:2000, α -tubulin (Sigma, T6199) at 1:500; in blocking solution overnight at 4°C, rinsed in DPBS, incubated with secondary Alexa Fluor 488 conjugated antibody (Invitrogen) in blocking solution (1:500) for 2 h and rinsed in DPBS. To label F-actin, fixed embryos were incubated with Phalloidin-Rhodamine (Molecular Probes, R415) at 1:500 and for nuclear staining with DAPI (Sigma, 10236276001) at 1:1000. For E-cad function blocking, embryos were treated with the DECMA-1 antibody (Sigma, U3254) or control IgG antibody (Sigma) at 1:500 in KSOM+AA.

As all suitable Pard6b antibodies (Alarcon, 2010; Hirate et al., 2015; Yamanaka et al., 2010) have recently been discontinued, the downregulation of Pard6b by siRNA was validated using quantitative RT-PCR. Total mRNA was extracted from pooled embryos using an Arcturus PicoPure Kit (Thermo Fisher) and RNase-Free DNase Set (QIAGEN). qRT-PCR was performed using a TaqMan RNA-to-CT 1-Step Kit (Thermo Fisher) and Lightcycler 480II qPCR (Roche). A TaqMan Gene Expression Assay (Thermo Fisher) was used to determine expression for *pard6b* (Mm00480520_m1).

For the dextran permeability assay, embryos were incubated in 40KDa Dextran-FITC (Sigma, FD40) at 25 ng μl^{-1} for 7 to 10 h starting prior to zippering and then washed in KSOM+AA. The embryos were imaged for FITC fluorescence in intracellular spaces. Positive detection of FITC indicates successful sealing.

Live embryo imaging

Live embryos were imaged using a laser scanning confocal (LSM 780 microscope, Zeiss) with water UV-VIS-IR Apochromat 63X 1.2 NA objective and highly sensitive avalanche photodiode light detectors of the Confocor 3 module (Zeiss). For FDAP experiments, photoactivation of paGFP-actin was performed using a 63X 1.20 objective and 820 nm two-photon laser (Mai Tai,

Spectra-Physics). A region of interest (ROI) of $5\ \mu\text{m} \times 10\ \mu\text{m}$ was scanned at 10% laser power in embryos labeled with RFP-Utr to identify the position of the ring. FRAP experiments were performed with a 63X 1.20 objective at 7X zoom magnification. A $4\ \mu\text{m} \times 4\ \mu\text{m}$ ROI was photobleached with 100% 488 nm laser power. Laser ablations were performed using a 63X 1.4 NA objective and multiphoton laser tuned to 790 nm and set to 50% laser power. Before and after ablation, $4\ \mu\text{m}$ thick confocal images were acquired at 5X magnification using avalanche photodiodes every 1.3 s on embryos expressing GFP-Utr. A $5\ \mu\text{m}$ line was scanned at $1\ \mu\text{s}$ pixel⁻¹ orthogonally across one section of the actin ring. PST-1P was used at 40 μM in KSOM+AA, embryos were incubated for 24 h in the dark before the start of the experiment. For PST-1P activation the Zeiss 63X 1.4 NA objective was used. A ROI was illuminated using 405 nm light, at 10% laser power for 2 s. For PST-1P deactivation the same ROI was illuminated using 514 nm light at 10% laser power for 2 s. Azido-blebbistatin was activated locally by illuminating a ROI ($3\ \mu\text{m} \times 5\ \mu\text{m}$) with a 405 nm laser at 20% laser power for 60 s. For photoactivation experiments, paGFP-actin was selectively photoactivated using a 820 nm multiphoton laser targeted to a defined ROI. Live-imaging was then used to visualize the photoactivated actin pool over time.

QUANTIFICATION AND STATISTICAL ANALYSIS

Image analysis

3D visualizations of embryos were performed using Imaris 8.2 software (Bitplane AG). The manual surface rendering module was used for cell segmentation. Cell volume and sphericity values were derived from the segmented data using the Imaris statistics module. Ring perimeter was measured using Imaris point measurement tool. The ring width was measured as the mean distance between the borders of the ring for 10 different positions using Imaris point measurement tool. The distance from the center of mass of the cell to the apical membrane was calculated using segmented data in Imaris. Quantification of immunofluorescence intensity and expression levels of E-cad-GFP, GFP- α -cat, Utr-GFP and GFP-actin were performed in ImageJ by measuring mean fluorescence intensity at a ROI. The fluorescence intensity profiles for GFP-actin, Phalloidin-Rhodamine, GFP-Utr and RFP-MAP2c were measured in ImageJ using a line width of 25 pixels along the apical cortex. To generate kymographs of paGFP-actin flow, a ROI was defined along the cortex in a 2D plane and straightened using ImageJ. M.B. acknowledges Bitplane AG for an Imaris Developer license.

EB3-dTomato tracking

The Imaris manual spot-detection module was used to analyze EB3-dTomato tracks (Yamashita et al., 2015). Only comets detected in at least 4 continuous time frames were used for analysis. Comets moving along the z axis were excluded from analysis. Number of EB3-dTomato labeled tracks were scored within 1 μm in a ROI of $3\ \mu\text{m} \times 3\ \mu\text{m}$ inside and outside the actin ring, and at the actin ring edge.

Curvature analysis

3D surface curvatures were calculated as described previously (Arora et al., 2016). Surfaces of post-mitotic cells were rendered in Imaris following segmentation. The vertices of these surface objects were transferred into MATLAB (MathWorks) and local 3D Gaussian and mean curvatures were calculated. These values were then transferred back into Imaris as statistical values associated with a spots object at each vertex via the Imaris XT MATLAB script (Arora et al., 2016). The script was modified to allow for signed curvatures, so as not to downsample the number of vertices or multiply curvatures values by a factor of 10. Radii calculated with six neighbor vertices are averaged. Curvatures (either Gaussian or mean) are displayed as a heatmap at each vertex, with the range indicated in the associated colorbar.

FDAP analysis

Mean fluorescence intensity of the photoactivated region was measured for every time point in ZEN (Zeiss). The mean intensity was corrected by background fluorescence and normalized for the intensity after photo-activation. The corrected data was fitted with a single exponential function.

$$I(t) = I(0)e^{-\frac{t}{\tau}} + I_{\infty}$$

Where, τ is the decay time and the immobile fraction is I_{∞} .

FRAP analysis

Mean fluorescence intensity at the photobleached region was corrected by background fluorescence and normalized to the mean intensity ratio between pre- and post-photobleaching from a non-bleached membrane region. The pre-bleaching intensity value was taken as 100%. Normalized fluorescence intensity ($I(t)$) data were fitted with a single exponential function:

$$I(t) = I(0) + (I_{\infty} - I(0))\left(1 - e^{-\frac{t}{\tau}}\right)$$

Where $I(0)$ is the fluorescence intensity immediately after bleaching, I_{∞} is the fluorescence intensity when the intensity reaches a plateau and τ is the characteristic time. The mobile fraction was calculated as $(I_{\infty} - I(0))/(1 - I(0))$ and the half time as $\tau \ln(2)$.

Laser ablation analysis

The initial recoil speed after ablation reflects tension at the targeted ring. Initial velocity was calculated as the distance of the gap detected immediately after ablation divided by the time since the ablation. We excluded from analysis cells damaged after ablation.

PIV analysis

High temporal resolution live imaging of GFP-Utr was used to visualize the dynamics of the F-actin flow. PIV analysis was performed for two consecutive frames at the same position throughout the duration of a movie. Flow profiles of the consecutive acquisition loops throughout the duration of a movie were subsequently averaged. Then magnitude of the mean velocity was calculated as a function of the position.

Statistical analysis

Analyses were performed with GraphPad Prism and MATLAB. Unpaired, two-tailed Student's *t* test was used, with the assumption of unequal variances. Reproducibility was confirmed by independent experiments. *n* represents cells, embryos, junctions or rings, as indicated in each figure legend.

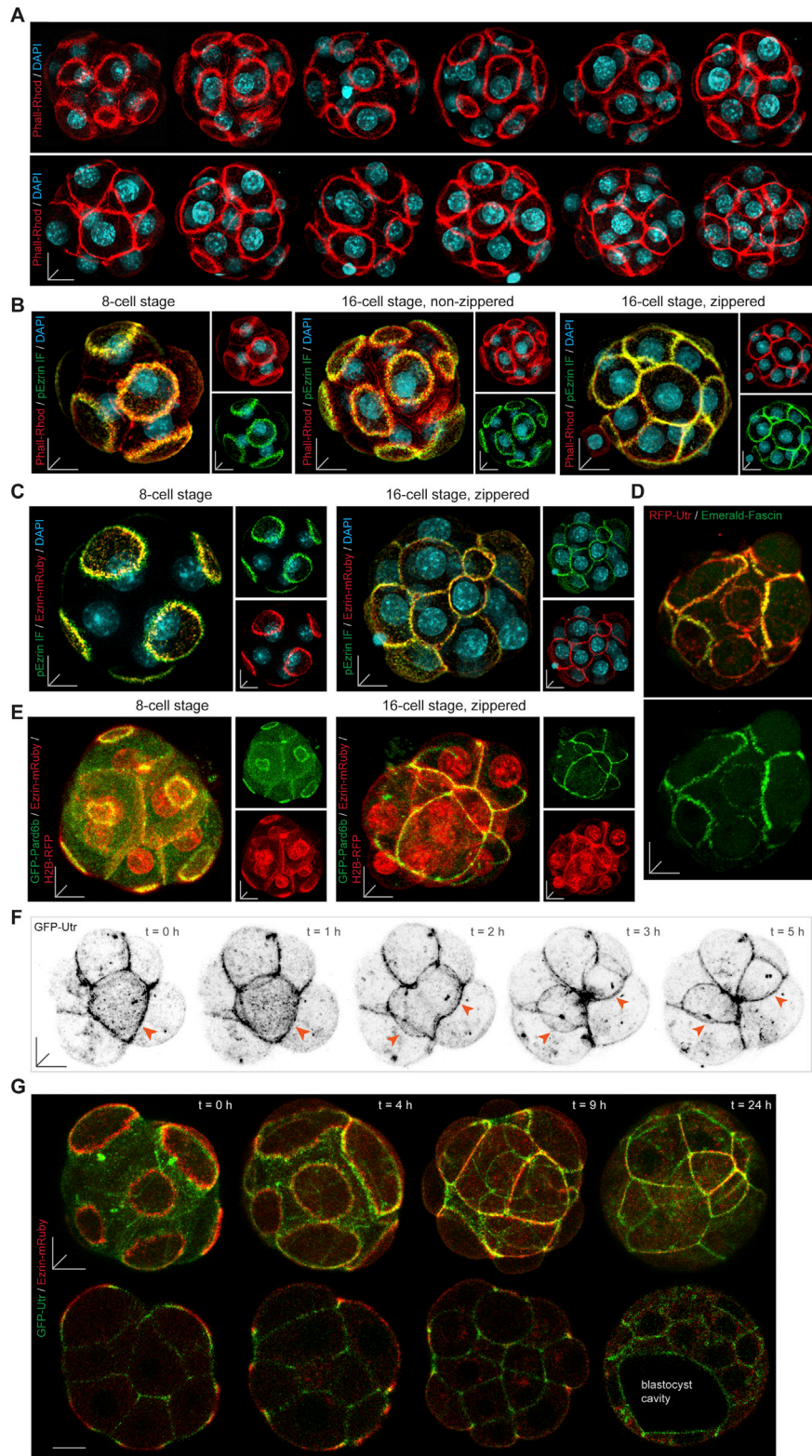


Figure S1. Actin Rings Are Labeled by Ezrin, Pard6b, and Fascin and They Remain Zippered during Division, Related to Figure 1

(A) Examples of non-injected 16- to 32-cell stage embryos stained with Phalloidin-Rhodamine and DAPI. The embryos are ordered left-to-right by developmental stage. Note the presence of actin rings at earlier stages and the retention of a zippered organization at more advanced stages.

(legend continued on next page)

(B) Immunofluorescence of 8-cell stage (left panel), early 16-cell stage (middle panel) and late 16-cell stage embryos (right panel) labeled for phosphorylated Ezrin (pEzrin), Phalloidin-Rhodamine and DAPI. pEzrin is specifically enriched at the ring of 8-cell embryos, non-zippered 16-cell embryos and along the zippered rings of late 16-cell embryos.

(C) Immunofluorescence of 8- and 16-cell stage embryos injected with Ezrin-mRuby at the 1-cell stage and labeled for pEzrin and DAPI. Ezrin-mRuby recapitulates the endogenous Ezrin staining.

(D) Localization of Emerald-Fascin at the actin ring of a live 16-cell embryo.

(E) Localization of GFP-Pard6b to the actin ring at the 8- and 16-cell stage in live embryos.

(F) Live imaging of a cell division in a 16-cell stage embryo expressing GFP-Utr. Arrowheads indicate the cell and its daughters preserving their zippered junctions throughout the division process.

(G) Live imaging of an embryo expressing GFP-Utr and Ezrin-mRuby shows expansion and zippering of the actin rings during the 16-cell stage, and maintenance of the zippered architecture as the blastocyst cavity forms, which is visible in the 2D panels.

Scale bars, 10 μm .

(E) Staining for phosphorylated Ezrin (pEzrin) or Phalloidin-Rhodamine and DAPI in fixed embryos shows disassembly of the cortical actin ring prior to cytokinesis (white arrowheads). 2D planes indicate the two daughter cells (yellow arrowheads).

(F) Live imaging of a cell division in an 8-cell stage embryo expressing RFP-Utr. White arrowheads indicate the ring disassembly prior to division. After cytokinesis, one daughter cell forms an actin ring *de novo* (orange arrowhead) while the other daughter cell does not form a ring (white arrowhead).

(G) Repetitive photoactivation of paGFP-actin at the cell cortex inside the actin ring (dashed box) of a live 16-cell stage blastomere shows no clear actin flow to the actin ring.

(H) Repetitive photoactivation of paGFP-actin at and near the nascent cell-cell junction (dashed box) of a live 16-cell stage blastomere. The images reveal a flow of cortical actin to the actin ring (arrowhead). Kymographs show the directional displacement of paGFP-actin and its accumulation at the actin ring.

(I) Live imaging of a 16-cell stage blastomere in an embryo expressing GFP-Utr treated with WGA immediately after cytokinesis of that cell. WGA treatment eliminates cortical flows and prevents actin ring formation. No cortical flow detected by PIV analysis (bottom panels).

(J) Graph shows fluorescence intensity of Phalloidin-Rhodamine along the cell cortex of a 16-cell stage blastomere (related to [Figure 2E](#)).

(K) Photoactivation and tracking of a selective pool of paGFP-actin along an actin ring (dashed box) during its expansion. Note that the photoactivated pool of paGFP-actin remains at the ring during expansion.

Data in (I) are presented as mean \pm SEM; scale bars, 10 μ m; n = cells.

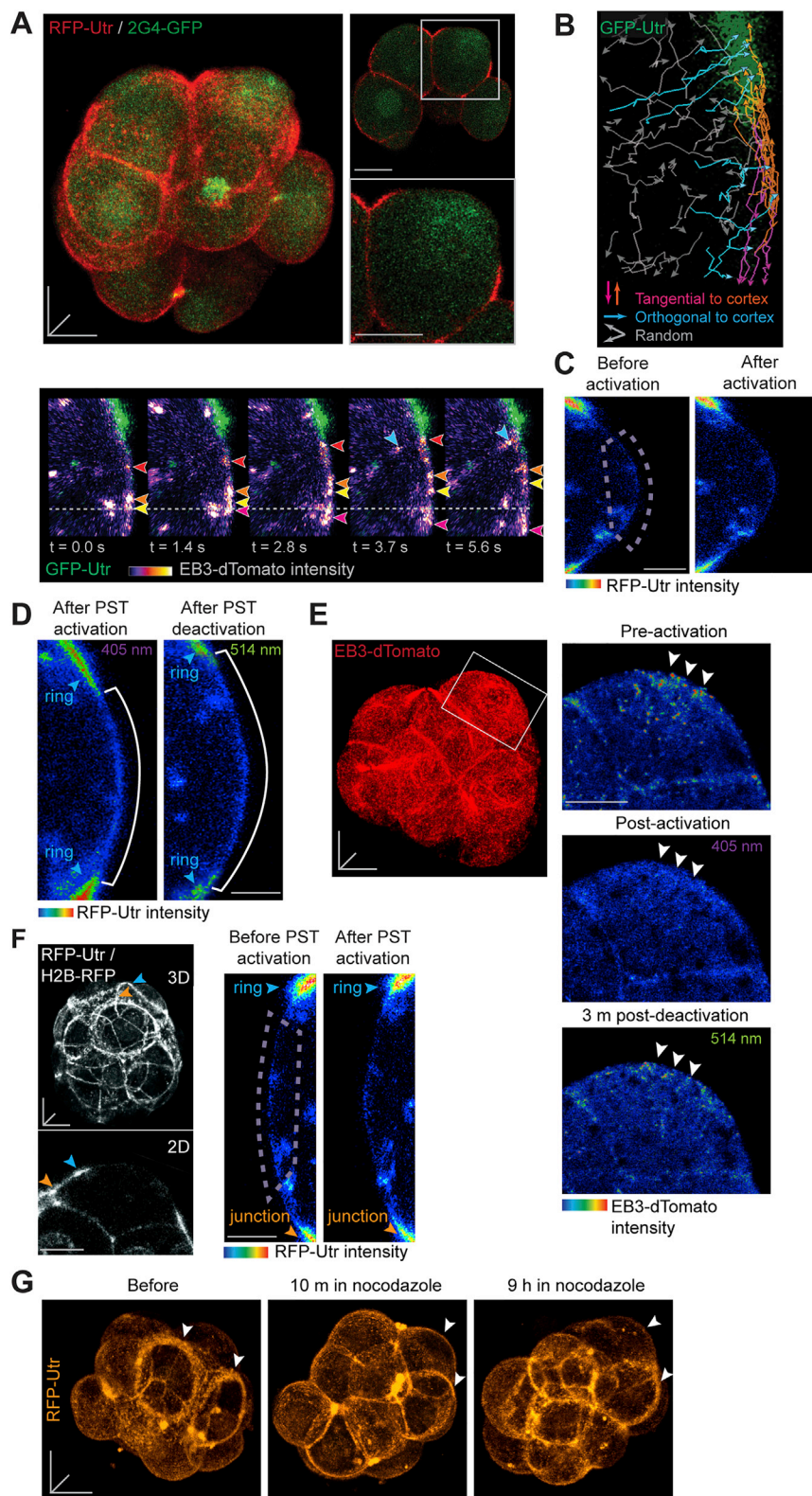


Figure S3. The Microtubule Network Underlying the Apical Cortex Is More Dynamic inside Than outside the Actin Ring, Related to Figure 3
 (A) Imaging of a forming ring in a live embryo expressing RFP-Utr and 2G4-GFP. Tyrosinated microtubules are mainly found under the cortex inside the ring, indicating a more dynamic network in this region.

(legend continued on next page)

(B) Tracking of EB3-dTomato labeled microtubule plus ends (colored arrows) in a 16-cell stage blastomere of a live embryo co-expressing GFP-Utr. Z-projection of all tracks reveals significantly more microtubule polymerization inside the ring than outside (upper right panel). Lower left panel shows individual tracks moving tangential to the cortex toward the edge of the ring (red, orange and yellow arrowheads), toward the center of the ring (pink arrowheads) or orthogonal to the cortex (blue arrowheads).

(C) 2D planes of a 16-cell stage blastomere in a live embryo incubated without PST. Localized photoactivation (dashed area) does not cause an accumulation of RFP-Utr inside the ring.

(D) PST deactivation of previously photoactivated PSTs results in a renewed clearance of RFP-Utr inside the ring (arrowheads).

(E) Live imaging of an embryo expressing EB3-dTomato incubated with PST. Localized PST activation and deactivation inside the actin ring causes loss and subsequent re-growth of microtubule plus-ends (arrowheads).

(F) Live imaging of an embryo expressing RFP-Utr and H2B-RFP incubated with PST. Localized PST activation (dashed area) outside the actin ring does not induce any change in RFP-Utr levels at the cortex.

(G) Live embryo expressing RFP-Utr before nocodazole treatment, 10 m and 9 h after nocodazole application. Nocodazole disrupts the GFP-Utr exclusion zone and prevents zippering (arrowheads).

Scale bars, 10 μm in all images except for lower panels in B, C, D, insets in F (3 μm).

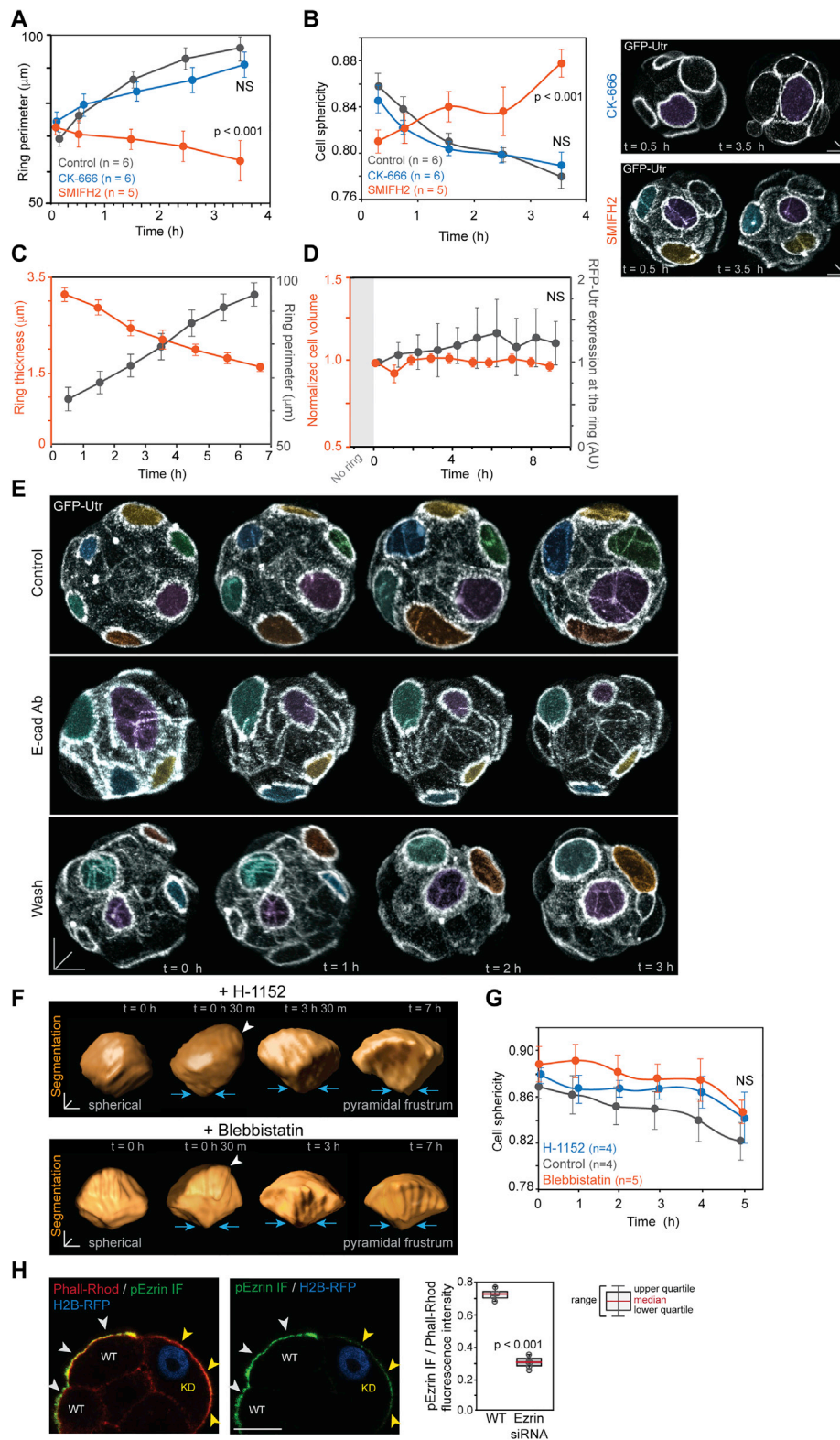


Figure S4. Actin Ring Size Changes with Cell Shape, Related to Figure 4

(A) Comparison of ring perimeter over time in 16-cell stage blastomeres of control embryos, embryos treated with Arp2/3 inhibitor CK-666 or pan-formin inhibitor SMIFH2.

(legend continued on next page)

(B) Cell sphericity is affected by SMIFH2 but not CK-666. Quantification and examples of embryos treated with CK-666 or SMIFH2.

(C) The thickness of the actin ring decreases as the ring expands.

(D) Quantification of cell volume and normalized total RFP-Utr levels at the ring during the 16-cell stage. T = 0 h indicates the time when the actin ring is formed.

(E) Comparison of live embryos expressing GFP-Utr treated with E-cad blocking antibody (E-cad Ab). E-cad Ab treatment induces shrinkage of actin rings (middle panel). The rings recover and expand normally after E-cad Ab washout (lower panel).

(F) Computational segmentation of a 16-cell stage blastomere of a living embryo treated with H-1152 or blebbistatin. The bulge inside the actin ring (white arrowhead) flattens as the cell changes from a spherical to a pyramidal frustum (arrows).

(G) H-1152 and blebbistatin do not prevent changes in cell shape assessed by quantification of cell sphericity.

(H) Immunofluorescence of a 16-cell stage embryo injected in one cell at 2-cell stage with RNA for H2B-RFP (pseudocolored) and siRNA against Ezrin. Embryos are labeled for phosphorylated Ezrin (pEzrin) and Phalloidin-Rhodamine. White arrowheads indicate the cortex of wild-type cells (WT) and yellow arrowheads indicate the cortex of a knockdown cell (KD). Graph shows quantification of pEzrin immunofluorescence intensity at the WT and the KD cortex.

Data in (A–D, G and H) are presented as mean \pm SEM; Scale bars, 10 μ m; n = embryos in G and cells elsewhere.

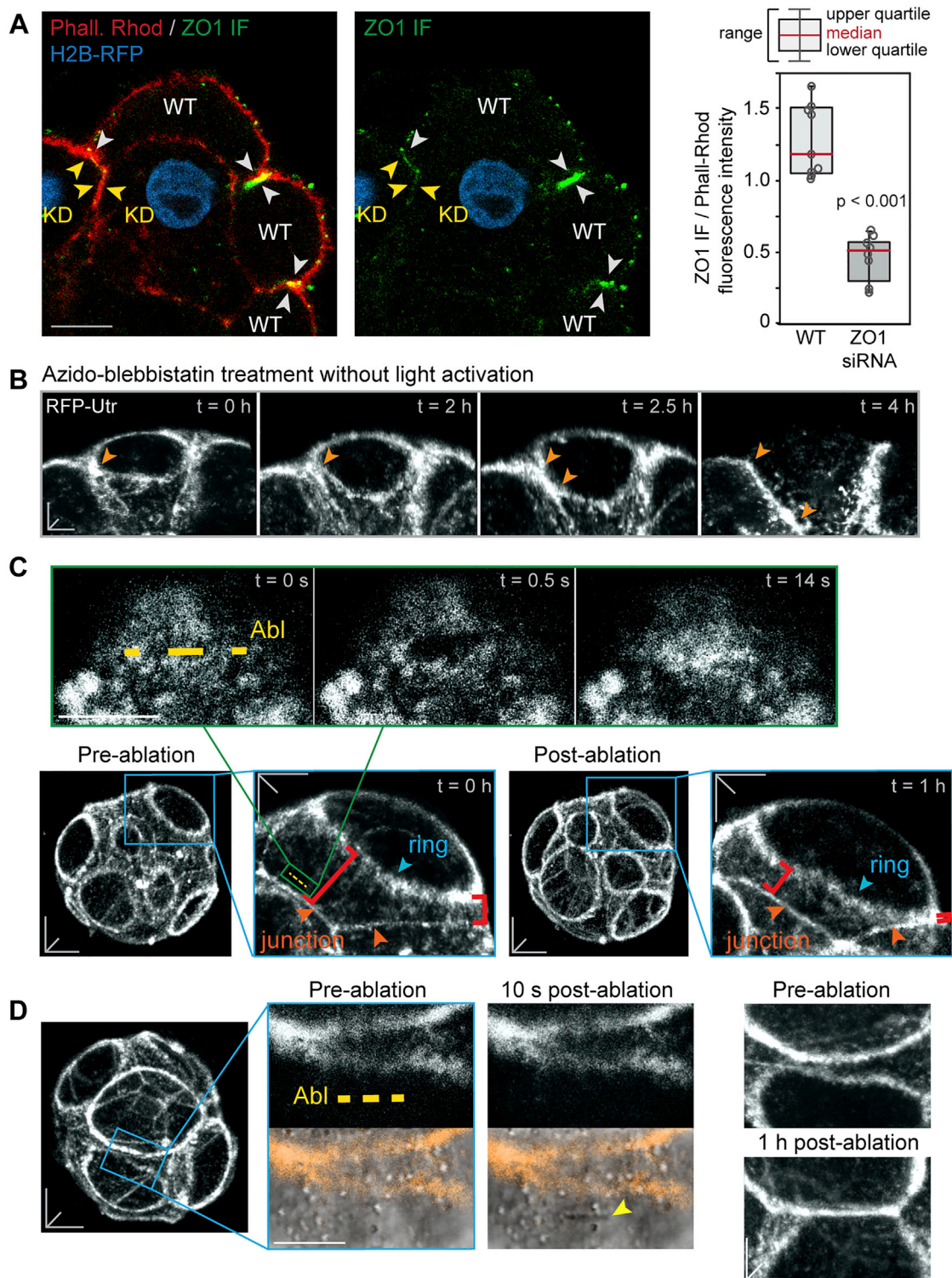


Figure S5. Control Experiments for ZO1 Knockdown, Azido-Blebbistatin Treatment, and Laser Ablations, Related to Figure 5

(A) Immunofluorescence of a 16-cell stage embryo injected in one cell at 2-cell stage with RNA for H2B-RFP (pseudocolored) and siRNA against ZO1. Embryos are immunostained for ZO1 and labeled with Phalloidin-Rhodamine. White arrowheads indicate junctions of wild-type cells (WT) and yellow arrowheads indicate junctions of knockdown cells (KD). Quantification of ZO1 immunofluorescence intensity at WT junctions and the KD junctions is shown in the right panel.

(B) Time-lapse imaging of 16-cell stage blastomeres of a live embryo expressing RFP-Utr, treated with azido-blebbistatin but without light activation. Arrowheads show neighboring actin rings coupling and zipping along the junction.

(legend continued on next page)

(C) Laser ablation (Abl, dashed line) of the cell cortex near a cell-cell junction at the time when an actin ring is still far away from that junction does not affect the subsequent expansion of the ring.

(D) Laser ablation at the cell cortex inside an expanding actin ring (dashed line and arrowhead) does not prevent its subsequent zippering (right panels).

Boxplots show median (red line), upper and lower quartile and range. Data in (A) are presented as mean \pm SEM; Scale bars, 10 μ m in all images except for insets in C and D (5 μ m); n = cells.

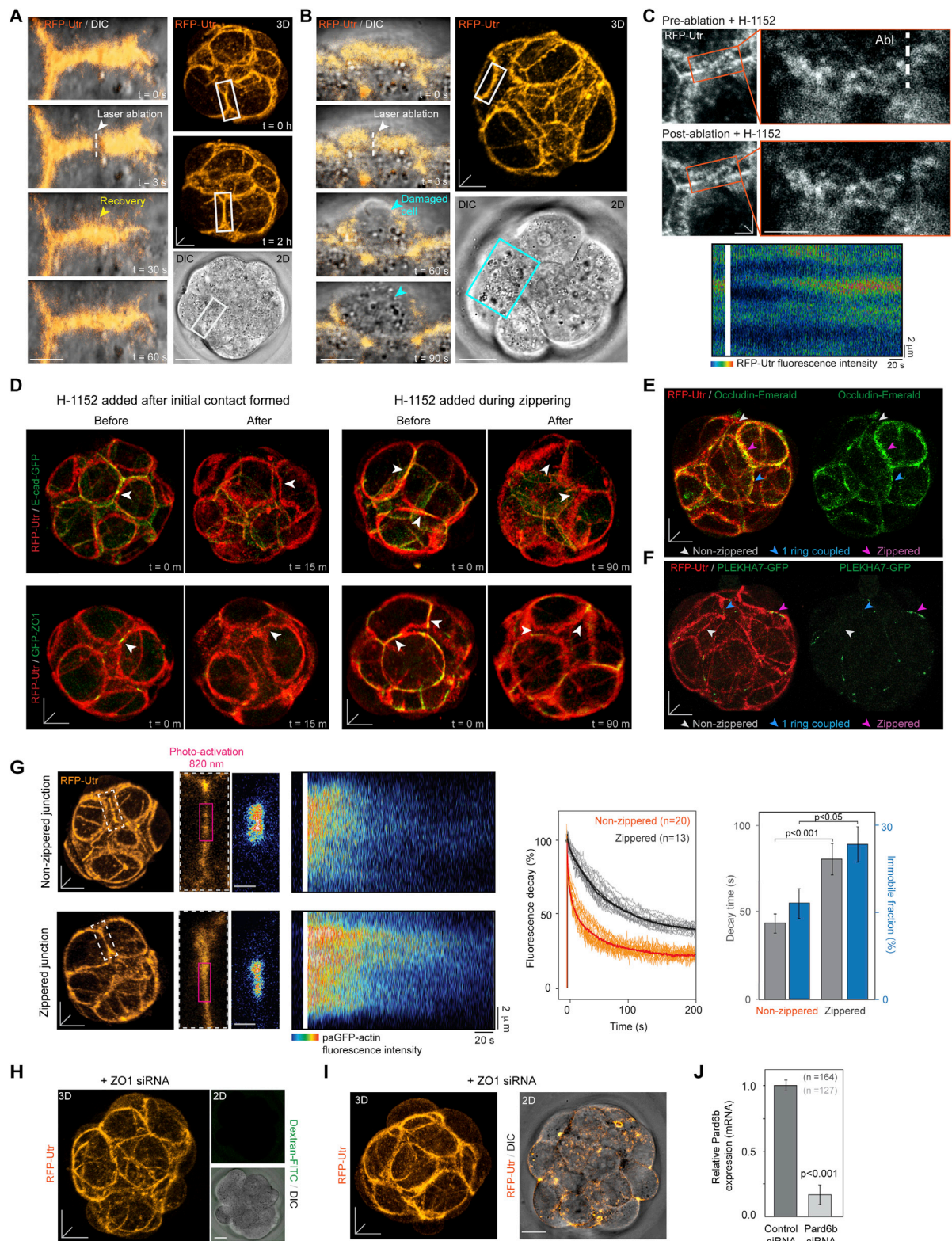


Figure S6. Laser Ablation Controls and Tight Junction Maturation following Actin Ring Coupling and Zippering, Related to Figures 5, 6, and 7
 (A) Laser ablation in a 16-cell stage embryo expressing RFP-Utr demonstrates recoil followed by recovery of RFP-Utr (left panels). After recovery, the ablated ring (white box) continues to zipper along the junction (right panels).

(legend continued on next page)

(B) Laser ablation causing cell damage is rapidly revealed by leakage of cytoplasmic material and the experiments are excluded from analysis (cyan arrowhead and box).

(C) Laser ablation of a zippered region in an embryo expressing RFP-Utr treated with H-1152 shows no recoil. Zoomed 2D views show the advancing zipper pre- and post-ablation. The minimal recoil response is observed in the kymograph.

(D) Live embryos expressing RFP-Utr and E-cad-GFP or GFP-ZO1. Treatment with H-1152 after formation of an initial point of contact between two rings causes uncoupling of the rings (left panels). Treatment during zippering leads to unzipping and uncoupling of actin rings (right panels).

(E and F) Live imaging of 16-cell stage embryos expressing RFP-Utr and Occludin-Emerald (E) or PLEKHA7-GFP (F) shows the recruitment of both markers along the zippering cell-cell junction. The arrowheads indicate the cell-cell junction before the first actin ring couples (white), after the first ring couples (blue), and after the second ring couples (magenta).

(G) FDAP analysis of paGFP-actin dynamics reveals a slower decay time and larger immobile fraction of paGFP-actin at zippered cell-cell junctions compared to non-zippered junctions.

(H and I) Downregulation of ZO1 prevents embryo sealing and blastocyst formation.

(J) Microinjection of Pard6b siRNAs at the 1-cell stage downregulates Pard6b expression at the 16-cell stage, as quantified by qPCR performed on embryo homogenates.

Data in (G and J) are presented as mean \pm SEM; Scale bars, 10 μ m in all images except for insets in A, B, C and G (3 μ m); n = junctions in G, embryos in J.